J. Mech. Phys. Solids 196 (2025) 106025

Contents lists available at ScienceDirect

Journal of the Mechanics and Physics of Solids

journal homepage: www.elsevier.com/locate/jmps

Gradient-enhanced ductile fracture constitutive modeling in implicit two-scale finite element analysis

Tianwen Tan, Ikumu Watanabe *

Graduate School of Pure and Applied Sciences, University of Tsukuba, 1-1-1 Tennodai, Tsukuba 305-8573, Japan
Center for Basic Research on Materials, National Institute for Materials Science, 1-2-1 Sengen, Tsukuba 305-0047, Japan

ARTICLE INFO

Keywords:
Ductile fracture
Mesh dependency
Micromorphic theory
Finite strains
Length scale

ABSTRACT

In the field of damage modeling for ductile materials, numerous models have successfully addressed various fracture responses, as well as the need for robust algorithms and solutions to computational challenges. This study developed a damage model based on continuum damage mechanics. It addresses mesh regularization, a primary computational issue in macroscopic structural fracture analysis through a gradient-enhanced damage model using micromorphic theory and incorporating damage hardening variables. To provide a physical explanation for the characteristic lengths associated with the gradient-enhanced term, an extended "two-scale" computational homogenization approach was employed to define the length scale between the macro- and microscale. This microvariable within a micromorphic extension can be utilized to model the damage hardening mechanism, which cannot be fully captured via high-resolution localized characterization. In duplex microstructures, the length scale can be defined by the microstructure size relative to the width of the micro-shear band. This explains the damage overlapping phenomenon between the two-scales.

1. Introduction

1.1. Background and aims

Crack initiation induced by damage accumulation and fracture processes are currently regarded as a challenging problem in solid mechanics. Computational tools can be utilized to conduct point-by-point analyses to predict structural failure across scales, which is challenging experimentally, thus contributing to reducing experimental costs in industrial applications. Automobile components and other products are made of ductile materials that undergo large elastoplastic deformation. Therefore, plastic deformation plays a critical role in failure processes. Approaches based on computational methods, such as the finite element method, must be controllable and exhibit high accuracy, even in the presence of coupling between "plasticity" and "damage" processes in ductile materials. Studies have established a solid foundation for modeling ductile materials, distinguishing between "decoupling" or "full coupling" in constitutive models with elastoplastic deformation and the damage mechanism (Besson, 2010; Brepols et al., 2020). The lack of a "coupling" property, often seen in works that focus solely on empirical or explicit failure criteria, raises concerns, particularly when materials experience complex loading paths and increasing damage processes (Johnson and Cook, 1985; Bao and Wierzbicki, 2004; Xue, 2007). Hence, this study prefers the full coupling approach, which is commonly classified into either "physical micromechanism-based" or "continuum damage mechanics-based" constitutive modeling (Besson, 2010). Based on the "physical

* Corresponding author at: Center for Basic Research on Materials, National Institute for Materials Science, 1-2-1 Sengen, Tsukuba 305-0047, Japan.
E-mail address: WATANABE.Ikumu@nims.go.jp (I. Watanabe).

https://doi.org/10.1016/j.jmps.2025.106025
Received 8 July 2024; Received in revised form 30 October 2024; Accepted 3 January 2025
Available online 8 January 2025

micromechanism" modeling approach, the Gurson–Tvergaard–Needleman (GTN) model (Tvergaard and Needleman, 1984) followed by Gurson (1977) describes a fracture mechanism involving microscopic voids that includes the evolution of void nucleation, growth, and linkage processes in consideration of the plastic volumetric effect and degradation on material strength. The decrease in stress (the damaged area experiences loading release) is related to an increasing volume fraction of microscopic voids. Essentially, this modeling can be explained by the homogenization theory between micro- and macro-scales. Certain works have been developed based on early research on the GTN model; these works consider the shear effect of microscopic voids (Xue, 2008; Nahshon and Hutchinson, 2008; Zhou et al., 2014) and damage characterization with phase-field fracture method and the absence of microscopic voids nucleation (Aldakheel et al., 2018). This study also considers the "Continuum damage mechanism" (CDM). The CDM is a phenomenological expression of the effective damage variable **D** in the macroscale, as either a scalar or tensor, that characterizes the anisotropy of damage (Lemaitre et al., 2000); it is similar to a ratio of effective and total loading surfaces. Most works using this approach achieve consistent thermodynamic results (Kachanov, 1958; Rabotnov, 1963; Chaboche, 1978) by assuming the effective property of non-damage solid and the hypothesis of strain equivalent (Lemaitre, 1984, 2012) as proposed by several researchers in the CDM community. This advantage of containing sufficient consistent thermodynamic dissipation with "plasticity" and "damage" modeling has been further developed and has improved the understanding of the opening(+)/closure(–) effects of microscopic cracks (Pires et al., 2003; Desmorat and Cantournet, 2008), extension to finite strain (de Souza Neto et al., 1998, 2011), and theoretical modeling via a "two-surface" approach for the independent mechanism between "plasticity" and "damage" (Simo and Ju, 1987; Voyiadjis and Kattan, 1992; Kattan and Voyiadjis, 2012; Watanabe et al., 2008; Voyiadjis et al., 2012).

However, the aforementioned coupling models have limitations. The "local" or "non-gradient" approach causes pathological and "fake" mesh dependencies induced by damaged material softening during finite element simulation at an engineering scale (Wriggers, 2008; Besson et al., 2009; De Borst et al., 2012; Voyiadjis and Song, 2020; Voyiadjis and Yaghoobi, 2019; Chen, 2019). This is particularly evident in different studies (Besson et al., 2009; Voyiadjis and Kattan, 2014), in which the damage-induced displacement (or strain) jump between neighboring elements can become significant with decreasing mesh refinement. Moreover, the damage zone and area of energy dissipation reach an extremely narrow region (De Borst et al., 1993, 2012; Neuner et al., 2020, 2022). In such cases, the numerical solution should be bounded with a decreasing mesh refinement. Different regularized approaches are available to resolve this problem in finite element simulations (Upadhyay et al., 2013; Neff et al., 2014). Bažant (1987) and Eringen (2001) concluded that the material response at a material point depends on not only itself but also points around it ("nonlocal" or "gradient–enhanced" approach). Firstly, the "nonlocal" models depend on the value of damage over a finite neighborhood of the point and include discontinuous and explicit methods, such as the extended finite element method (Moës and Belytschko, 2002) and nonlocal integral method as well as its Taylor series approximation with certain weight functions (Bazant et al., 1984; Bazant and Pijaudier-Cabot, 1988; Leblond et al., 1994). However, these methods have known issues, namely, the need for a predetermined crack path and the complexities involved in their implementation. Secondly, the "gradient–enhanced" models depend only on variables defined within an infinitesimal neighborhood of the point before spatial discretization. They require a continuity property with implicit time integration. These models include the implicit gradient approach (Peerlings et al., 1995, 1998), phase field method (Miehe et al., 2015; Ambati et al., 2016), gradient-enhanced damage energy theory (Zhang et al., 2018), and micromorphic theory (Forest, 2009, 2016; Diamantopoulou et al., 2017), all of which achieve high thermodynamic consistency. Hence, the present work focuses on gradient enhancement to damage based on the micromorphic theory. The advantage of micromorphic theory is that it models from a homogenization theory perspective (Hütter, 2017; Ling et al., 2018), which confers the ability to provide more detailed physical meanings of the characteristic length in the "gradient–enhanced" category, a micromorphic concept, which includes the additional global equilibrium into a resolved partial differential equation (PDE) for damage gradient extension. The complete modeling, from theory to the implementation, of a micromorphic extension to the effective damage variable D with a "two-surface" consideration was proposed by Dimitrijevic and Hackl (2011), Kiefer et al. (2018), Sprave and Menzel (2020, 2023), Brepols et al. (2020), and Felder et al. (2022). Moreover, Aslan et al. (2011a) and Aslan et al. (2011b) developed a micromorphic extension in which damage is coupled to single crystal plasticity. Therefore, the "two-surface" and micromorphic extensions to damage hardening variables warrant further research and are developed in the current work. This study follows previous research on the non-gradient approach (Watanabe et al., 2008) and emphasizes that "plasticity" and "damage" mechanisms can independently and implicitly interact with each other.

With the application of "two-surface" ductile damage modeling and micromorphic extension, the proposed model can be utilized not only for mesh regularization but also for deeper characterization at the microscale. Therefore, the difficulty of the definition and reasonable physical explanation of micromorphic material constants should be investigated. This concept has often been ignored in previous works, which has increased the difficulty of re-implementation in ductile fracture analysis and the proposed solutions have seemed to lack connection with experimental characterizations. As the second objective of the current work, a homogenization approach in ductile fracture analysis that can be considered to have a similar size effect within transient/dynamic effects in inertial problems (de Souza Neto et al., 2015) and transient thermal problems (Pham et al., 2013; Waseem et al., 2020) was developed. This approach should only be considered when there is a micromorphic extension to the damage hardening variable, similar to the gradient plasticity discussed in Ling et al. (2018). It involves defining a specific length scale between submicroscopic, microscopic, and macroscopic characteristic lengths, and establishing a reasonable physical meaning for micromorphic material parameters derived from the magnitude of scale overlapping between the microscale and macroscale.

1.2. Structure of the present work

Section 2 presents all the constitutive formulations of material modeling with thermodynamic consistency to compare the "non-gradient" and "micromorphic" models. Section 3, using the inherent strong and weak forms formulated in Section 2, discusses the fully implicit numerical implementation via the finite element method, as well as the stress update algorithm, its related consistent tangent matrices, and the material constitutive behavior at the material point level. Section 4 presents numerical examples across the macroscale and microscales to verify the mesh regularization and definition of length scale, as well as an explanation of the extended homogenized approach in ductile fracture analysis. Section 5 presents the conclusions.

2. Constitutive modeling and formulations

2.1. Kinematics of finite strain elastoplasticity with damage

The deformation gradient can be multiplicatively split into elastic $\mathbf{F}^{\mathrm{e}}$ and plastic $\mathbf{F}^{\mathrm{p}}$ (Figure 1 of Watanabe et al. (2008)), which allows for the kinematics of elastoplastic damageable materials to be described in terms of classical elastoplastic materials.

$$\mathbf{F} = \nabla_{\boldsymbol{X}}\mathbf{u} := \mathbf{F}^{\mathrm{e}}\mathbf{F}^{\mathrm{p}} \tag{1}$$

The frame transformation from material to spatial configuration can be explained in three steps: material (reference), plastic intermediate, and spatial (current). The detailed physical interpretations of these individual deformation gradients relate to different characterizations of microscopic mechanisms. For example, the plastic term results from plastic deformation accumulating via inelastic slip on different crystallographic slip systems, whereas the elastic term accounts for crystal lattice stretch and rotation. The result based on different configurations should be the same, at least in theory. These transformations also emphasize the distinctive structures of formulations from different configurations.

2.2. Consistent thermodynamic formulations

First, in constitutive modeling, the formulations are simultaneously presented to highlight a significant point between the previous finite strain elastoplastic-damage model proposed by Watanabe et al. (2008) and the proposed micromorphic extended model.

By considering the power associated with arbitrary kinematics and applying the divergence theorem to classical linear momentum equilibrium, the internal power density $\mathrm{W}_0^{\mathrm{int}}$ can be defined in the reference configuration using Eq. (2), represented by either $\mathbf{P} : \dot{\mathbf{F}}$ or $\mathbf{S} : \dot{\mathbf{E}}$, as the internal strain–energy rate. However, for the second thermodynamic law under isothermal conditions, the solid (analyzed domain) should not violate $\left(\mathrm{W}_0^{\mathrm{int}} - \rho\dot{\Psi} \geq 0\right)$ where ρ is the density and Ψ contains Helmholtz free energies.

Non − gradient :

$$\begin{aligned}\mathrm{W}_0^{\mathrm{int}} - \rho\dot{\Psi} &= \mathbf{P} : \dot{\mathbf{F}} - \rho\dot{\Psi}\left(\mathbf{C}^{\mathrm{e}}, \mathrm{D}, \xi, \eta\right)\\ &= \mathbf{S} : \dot{\mathbf{E}} - \rho\left(2\frac{\partial\Psi}{\partial\mathbf{C}^{\mathrm{e}}} : \frac{1}{2}\dot{\mathbf{C}}^{\mathrm{e}} + \frac{\partial\Psi}{\partial\xi}\dot{\xi} + \frac{\partial\Psi}{\partial\mathrm{D}}\dot{\mathrm{D}} + \frac{\partial\Psi}{\partial\eta}\dot{\eta}\right)\end{aligned} \tag{2}$$

Hence, the second form of the thermodynamic inequality in Eq. (2) is used further, where $\mathbf{P}/\mathbf{S}$ represents the first/second Piola–Kirchhoff stress, and $\mathbf{E}$ is the Green–Lagrange strain tensor, both defined in the reference configuration. The elastic left Cauchy–Green tensor $\mathbf{C}^{\mathrm{e}} = \mathbf{F}^{\mathrm{eT}}\mathbf{F}^{\mathrm{e}}$, isotropic plastic hardening variable ξ, effective damage variable D, and isotropic damage hardening variable η are internal state variables from the "non-gradient" model (Watanabe et al., 2008).

According to Watanabe et al. (2008) and Note 1, applying the effective damage variable D and isotropic damage hardening variable η can characterize material stiffness and strength degradation. The micromorphic extension, considering regularization with respect to the damage hardening variable η, was derived based on the discussion in Note 2.

Micromorphic :

$$\begin{aligned}\mathrm{W}_0^{\mathrm{int}} - \rho\dot{\Psi} &= \mathbf{P} : \dot{\mathbf{F}} + a^{\mathrm{m}}\dot{\tilde{\eta}} + \mathbf{b}^{\mathrm{m}} \cdot \nabla_{\boldsymbol{X}}\dot{\tilde{\eta}} - \rho\dot{\Psi}\left(\mathbf{C}^{\mathrm{e}}, \tilde{\eta}, \nabla_{\boldsymbol{X}}\tilde{\eta}, \mathrm{D}, \xi, \eta\right)\\ &= \mathbf{S} : \dot{\mathbf{E}} + a^{\mathrm{m}}\dot{\tilde{\eta}} + \mathbf{b}^{\mathrm{m}} \cdot \nabla_{\boldsymbol{X}}\dot{\tilde{\eta}}\\ &\quad - \rho\left(2\frac{\partial\Psi}{\partial\mathbf{C}^{\mathrm{e}}} : \frac{1}{2}\dot{\mathbf{C}}^{\mathrm{e}} + \frac{\partial\Psi}{\partial\xi}\dot{\xi} + \frac{\partial\Psi}{\partial\mathrm{D}}\dot{\mathrm{D}} + \frac{\partial\Psi}{\partial\eta}\dot{\eta} + \frac{\partial\Psi}{\partial\tilde{\eta}}\dot{\tilde{\eta}} + \frac{\partial\Psi}{\partial\nabla_{\boldsymbol{X}}\tilde{\eta}} \cdot \nabla_{\boldsymbol{X}}\dot{\tilde{\eta}}\right)\end{aligned} \tag{3}$$

The difference between Eqs. (2) and (3) includes two additional terms within the expression of the internal power density $\mathrm{W}_0^{\mathrm{int}}$, owing to the inclusion of terms for micromorphic global equilibrium and micromorphic Helmholtz free energy Ψ in Eq. (3), which contains the coupling term and gradient enhancement.

Note 1. The internal strain energy density is the same as the classical finite strain elasto-plasticity problem; however, it considers undamaged $(\bullet)^*$ to damaged $(\bullet)$ quantities. Owing to the scalar effective damage variable D under isotropic condition, the frame

definition of the damage variable is unclear or frame-independent. The aforementioned non-gradient model can contain several possible processes, including hyperelastic, hyperelastoplastic, hyperelasto-damage, and hyperelastoplastic-damage cases. In these cases, the evolutions of internal variables D and η are not necessarily the same; the Helmholtz free energy $\Psi(\mathbf{C}^{\mathrm{e}}, \mathrm{D}, \xi, \eta)$ presented the most general case.

Note 2. The challenge lies in determining which variable in Eq. (2) should be regularized in the constitutive modeling. For example, the damage regularization with the effective damage variable D has been bounded (Brepols et al., 2020) and not bounded (Kiefer et al., 2018). A similar micromorphic-extension to that discussed in Ling et al. (2018) was used, involving a micromorphic extension on the single crystal gradient-plasticity with respect to the accumulated plastic strain from microscopic slips and additional isotropic plastic hardening term with a Laplacian to characterize the microscopic mechanism owing to microscopic slips. Thus, the internal power density should be extended, including a coupled term a^{m} between the standard damage hardening variable η and the micromorphic damage hardening variable $\tilde{\eta}$ as well as the gradient-enhancement. The $\tilde{\eta}$ term should be defined with a configuration-property owing to the interpolation of the micromorphic damage gradient $\mathbf{b}^{\mathrm{m}}$. The difference in formulations is significant (Forest, 2016). All advantages discussed in Note 1 are inherent too, with the only enhancement stemming from the microscopic damage mechanism term $\partial\Psi/\partial\eta$ in Eq. (3).

To obtain the complete dissipation inequality, certain representative operations with respect to the frame transformations of second-order tensors are required,

$$\begin{aligned} &\mathbf{S} = \mathbf{F}^{\mathrm{p}-1}\hat{\mathbf{S}}^{\mathrm{e}}\mathbf{F}^{\mathrm{p}-\mathrm{T}}, \qquad \mathbf{E} = \frac{1}{2}(\mathbf{C}-\mathbf{1}), \quad \mathbf{C} = \mathbf{F}^{\mathrm{T}}\mathbf{F} \\ &\dot{\mathbf{E}} = \frac{1}{2}\overset{\cdot}{\left(\mathbf{F}^{\mathrm{p}\mathrm{T}}\mathbf{C}^{\mathrm{e}}\mathbf{F}^{\mathrm{p}}\right)} = \frac{1}{2}\left(\dot{\mathbf{F}}^{\mathrm{p}\mathrm{T}}\mathbf{C}^{\mathrm{e}}\mathbf{F}^{\mathrm{p}} + \mathbf{F}^{\mathrm{p}\mathrm{T}}\mathbf{C}^{\mathrm{e}}\dot{\mathbf{F}}^{\mathrm{p}} + \mathbf{F}^{\mathrm{p}\mathrm{T}}\dot{\mathbf{C}}^{\mathrm{e}}\mathbf{F}^{\mathrm{p}}\right) \end{aligned} \tag{4}$$

The second Piola–Kirchhoff stress $\mathbf{S}$ on the reference configuration Ω_0 can be transferred to the elastic term $\hat{\mathbf{S}}^{\mathrm{e}}$ defined on the plastic intermediate configuration Ω_{p}. Additionally, the strain measurement $\mathbf{E}$ on Ω_0 was defined and can be transferred to $\mathbf{E}^{\mathrm{e}}$ on Ω_{p}. Combining Eqs. (3) and (4) with assumptions including the effective quantities yields a relation with damaged terms, such as $\mathbf{S}^{*} = \mathbf{S}/f(\mathrm{D})$, with a hypothesis of strain equivalence. Moreover, the Helmholtz free energy has an additive expression, that is, "$\Psi = \Psi^{\mathrm{e}}(\mathbf{C}^{\mathrm{e}}, \mathrm{D}) + \Psi^{\mathrm{p}}(\xi, \mathrm{D}) + \Psi^{\mathrm{d}}(\eta) + \Psi^{\mathrm{m}}\left(\eta, \tilde{\eta}, \nabla_{\boldsymbol{X}}\tilde{\eta}\right)$" in Eq. (3). The full Clausius–Duhem inequality, following the micromorphic theory (Forest, 2009), was derived below:

Micromorphic :

$$\begin{aligned} &\left(\hat{\mathbf{S}}^{\mathrm{e}} - 2\frac{\partial\Psi^{\mathrm{e}}}{\partial\mathbf{C}^{\mathrm{e}}}\right) : \dot{\mathbf{E}}^{\mathrm{e}} + \left(a^{\mathrm{m}} - \frac{\partial\Psi^{\mathrm{m}}}{\partial\tilde{\eta}}\right)\dot{\tilde{\eta}} + \left(\mathbf{b}^{\mathrm{m}} - \frac{\partial\Psi^{\mathrm{m}}}{\partial\nabla_{\boldsymbol{X}}\tilde{\eta}}\right)\cdot\nabla_{\boldsymbol{X}}\dot{\tilde{\eta}} \\ &\quad + \left(2\mathbf{C}^{\mathrm{e}}\frac{\partial\Psi^{\mathrm{e}}}{\partial\mathbf{C}^{\mathrm{e}}}\right) : \dot{\mathbf{F}}^{\mathrm{p}}\mathbf{F}^{\mathrm{p}-1} - \frac{\partial\Psi^{\mathrm{p}}}{\partial\xi}\dot{\xi} + \left(-\frac{\partial\left(\Psi^{\mathrm{e}}+\Psi^{\mathrm{p}}\right)}{\partial\mathrm{D}}\right)\dot{\mathrm{D}} - \frac{\partial\left(\Psi^{\mathrm{d}}+\Psi^{\mathrm{m}}\right)}{\partial\eta}\dot{\eta} \qquad \geq 0 \end{aligned} \tag{5}$$

The micromorphic damage hardening variable can be regarded as a scalar micromorphic variable, owing to the coupling term $a^{\mathrm{m}}\dot{\tilde{\eta}}$ and gradient term $\mathbf{b}^{\mathrm{m}}\cdot\nabla_{\boldsymbol{X}}\dot{\tilde{\eta}}$, the assumption for pure-energetic micromorphic conjugate forces used in this work; however, the dissipative term can be extended as discussed in Gurtin (2002) and Ohno and Okumura (2007). The reduced dissipation inequality about the "non-gradient" in Eq. (6) and the micromorphic model in Eq. (7) can be obtained using the Coleman–Noll procedure.

$$\textbf{non}-\textbf{gradient} \qquad \hat{\mathbf{M}}^{\mathrm{e}} : \mathbf{L}^{\mathrm{p}} - \tau_{\mathrm{c}}\dot{\xi} + Y^{\mathrm{d}}\dot{\mathrm{D}} - \underline{\beta^{\mathrm{d}}\dot{\eta}} \geq 0 \tag{6}$$

$$\textbf{Micromorphic} \qquad \hat{\mathbf{M}}^{\mathrm{e}} : \mathbf{L}^{\mathrm{p}} - \tau_{\mathrm{c}}\dot{\xi} + Y^{\mathrm{d}}\dot{\mathrm{D}} - \underline{\beta^{\mathrm{m}}\dot{\eta}} \geq 0 \tag{7}$$

Additionally, the thermodynamic conjugate forces are derived as follows.

$$\textbf{Derivation} : \begin{cases} \hat{\mathbf{S}}^{\mathrm{e}} = 2\dfrac{\partial\Psi^{\mathrm{e}}}{\partial\mathbf{C}^{\mathrm{e}}}; & \tau_{\mathrm{c}} = \dfrac{\partial\Psi^{\mathrm{p}}}{\partial\xi} \\ \hat{\mathbf{M}}^{\mathrm{e}} = \mathbf{C}^{\mathrm{e}}\hat{\mathbf{S}}^{\mathrm{e}}; & \mathbf{L}^{\mathrm{p}} = \dot{\mathbf{F}}^{\mathrm{p}}\mathbf{F}^{\mathrm{p}-1} \\ a^{\mathrm{m}} = \dfrac{\partial\Psi^{\mathrm{m}}}{\partial\tilde{\eta}}; & Y^{\mathrm{d}} = \left(-\dfrac{\partial\left(\Psi^{\mathrm{e}}+\Psi^{\mathrm{p}}\right)}{\partial\mathrm{D}}\right) \\ \mathbf{b}^{\mathrm{m}} = \dfrac{\partial\Psi^{\mathrm{m}}}{\partial\nabla_{\boldsymbol{X}}\tilde{\eta}}; & \beta^{\mathrm{m}} = \beta^{\mathrm{d}} + \beta^{\mathrm{e}} = \dfrac{\partial\Psi^{\mathrm{d}}}{\partial\eta} + \dfrac{\partial\Psi^{\mathrm{m}}}{\partial\eta} \end{cases} \tag{8}$$

The tensor contraction between the asymmetric elastic Mandel stress $\hat{\mathbf{M}}^{\mathrm{e}}$ and the asymmetric plastic velocity gradient $\mathbf{L}^{\mathrm{p}}$ is maintained. In addition, the plastic resistances τ_{c} should be modeled from the statistical microscopic plastic mechanism. However, regarding damage dissipation, the Y^{d} term, as the damage norm (or energy release rate) including the elastic and plastic contributions, should be conjugated with the evolution of the effective damage variable D. Using the same perspective as that of plastic hardening, it is reasonable to model the damage hardening phenomena from a specific microscopic damage mechanism in the standard term β^{d} and the micromorphic term β^{e}. The comparison and reason why the isotropic damage hardening variable η is selected as the gradient term are discussed in Note 3. This finite strain elastoplastic micromorphic damage problem can be expressed as elastoplasticity on the intermediate and damage on the reference configuration.

Note 3. The comparison between Eqs. (6) and (7) should be emphasized by intrinsic and micromorphic-extended properties, including the damage norm Y_{d} and isotropic damage hardening term β^{x}. Despite these different micromorphic extensions, in which either Y^{d} or β^{d} can be equivalent under suitable assumptions, they significantly differ in terms of the characterization of microscopic damage mechanisms, similar to the isotropic plastic strain gradient hardening in single crystal micromorphic plasticity as discussed in Aifantis (1987), Aslan et al. (2011b), and Ling et al. (2018).

2.3. Plasticity modeling

To maintain the reduced energy dissipation in Eqs. (6) and (7), we used Lagrangian optimization to maximize dissipation for the evolution of the internal variables: the plastic flow rule $\mathbf{L}^{\mathrm{p}}$ and rates of the effective plastic strain $\dot{\varepsilon}^{\mathrm{p}}_{\mathrm{eq}}$, effective damage variable $\dot{\mathrm{D}}$, plastic hardening variable $\dot{\xi}$, and standard damage hardening variable $\dot{\eta}$. The relation between the $\hat{\mathbf{M}}^{\mathrm{e}}$ and $\mathbf{L}^{\mathrm{p}}$ is transferred into one between the effective stress norm $|\tau_{\mathrm{r}}|\mathrm{sign}(\tau_{\mathrm{r}})$ and equivalent plastic strain rate $\dot{\xi}$ using the plastic flow tensor $\mathbf{N}^{\mathrm{p}}$ under the strain–hardening mechanism. Simultaneously, the relation of damage can be transferred into a relation between the damage norm Y^{d} and the effective damage variable rate $\dot{\mathrm{D}}$. The effective quantities are defined by the damage contribution within "$\hat{\mathbf{M}}^{\mathrm{e}} = f(\mathrm{D})\hat{\mathbf{M}}^{\mathrm{e}*}$" and "$\tau_{\mathrm{c}} = h(\mathrm{D})\tau^{*}_{\mathrm{c}}$" about the elastic and plastic degradation functions $f(\mathrm{D})$ and $h(\mathrm{D})$, which are defined in terms of the Helmholtz free energies in Eqs. (3) and (8).

The components of the reduced energy dissipation can be rewritten as follows.

$$\mathbf{L}^{\mathrm{p}} = \dot{\mathbf{F}}^{\mathrm{p}}\mathbf{F}^{\mathrm{p}-1} \Rightarrow \dot{\varepsilon}^{\mathrm{p}}_{\mathrm{eq}}\mathbf{N}^{\mathrm{p}} \quad .\mathrm{or}. \quad \gamma_{\mathrm{p}}\mathbf{N}^{\mathrm{p}} \tag{9}$$

$$\hat{\mathbf{M}}^{\mathrm{e}} : \mathbf{L}^{\mathrm{p}} \Rightarrow \hat{\mathbf{M}}^{\mathrm{e}} : \gamma_{\mathrm{p}}\mathbf{N}^{\mathrm{p}} = \left(\hat{\mathbf{M}}^{\mathrm{e}} : \mathbf{N}^{\mathrm{p}}\right)\gamma_{\mathrm{p}} \tag{10}$$

With the requirement of reduced dissipative inequality, the resolved shear stress norm $\tau_{\mathrm{r}} = \left(\hat{\mathbf{M}}^{\mathrm{e}} : \mathbf{N}^{\mathrm{p}}\right)$ should be the same as the equivalent plastic strain rate $\dot{\xi}$, which corresponds to the correct movement of the slip system regarding "$\mathrm{sign}(\tau_{\mathrm{r}}) = \mathrm{sign}(\dot{\xi})$". After integrating formulations in the plastic intermediate configuration and back to the reference configuration, the yield function $\boldsymbol{\Phi}^{\mathrm{p}}$ for plasticity can be derived along with the application of Lagrangian optimization to maximize the plastic dissipation via an internal Lagrangian multiplier γ_{p}.

$$\boldsymbol{\Phi}^{\mathrm{p}} = |\tau_{\mathrm{r}}| - \tau_{\mathrm{c}} = f(\mathrm{D})|\tau^{*}_{\mathrm{r}}| - h(\mathrm{D})\tau^{*}_{\mathrm{c}} \tag{11}$$

The Karush–Kuhn–Tucker conditions of plasticity need to be considered.

$$\gamma_{\mathrm{p}} \geq 0, \quad \boldsymbol{\Phi}^{\mathrm{p}} \leq 0, \quad \gamma_{\mathrm{p}}\boldsymbol{\Phi}^{\mathrm{p}} = 0 \tag{12}$$

The evolution of plasticity-related variables can be derived. Details follow in terms of damage in Eqs. (20)–(22).

$$\dot{\varepsilon}^{\mathrm{p}}_{\mathrm{eq}} = \gamma_{\mathrm{p}}; \quad \dot{\xi} = \gamma_{\mathrm{p}}; \tag{13}$$

Note 4. The reduced dissipation inequality of the plastic part on the intermediate configuration is general in plasticity theory. Various plasticity models can be derived based on different expressions of these quantities and the objective function of the optimization. This model will be reduced to the classical plasticity model when no damage occurs. This proposed plasticity modeling on the intermediate configuration is only correct preliminarily, with the gradient term of micromorphic damage hardening being defined on the reference or spatial configuration.

2.4. Damage modeling

According to the material modeling of damage under finite strain, the difference between the definitions of micromorphic damage among configurations is discussed above, and the energy in Eq. (3) is considered. A difference exists in the efficiency of regularization related to the gradients of regularized variables in Wcisło et al. (2013). Moreover, this study focuses on the difference between the non-gradient damage model and the proposed extended model of the micromorphic damage hardening variables $\tilde{\eta}$.

2.4.1. Damage modeling: global controlling equilibriums

As primary damage modeling, it must focus on the applying the principle of virtual work. There are two lemmas: "the external virtual work must be equal to internal virtual work in the static or quasi-static system during the time variation" (lemma 1), and "the assumed or derived virtual internal work must satisfy frame-invariant property during the changed frame on spatial configuration" (lemma 2) emphasized in Gurtin et al. (2010). As demonstrated in expressions of the internal power density in Eqs. (2) and (3), the application of lemma 1 with equality between the internal $\delta \mathrm{W}^{\mathrm{int}}_{0}$ and external $\delta \mathrm{W}^{\mathrm{ext}}_{0}$ virtual work variation with time is considered.

The derivation of lemma 1 in which follows:

$$\underbrace{\int_{\Omega_0} \mathbf{S} : \delta\mathbf{E}\, \mathrm{d}V - \int_{\Omega_0} \mathbf{f}_0 \cdot \delta\mathbf{u}\, \mathrm{d}V - \int_{\partial\Omega^{\mathrm{t}}_0} \mathbf{t}_0 \cdot \delta\mathbf{u}\, \mathrm{d}A}_{\textbf{Non-gradient}} + \underbrace{\int_{\Omega_0} \left(a^{\mathrm{m}}\delta\tilde{\eta} + \mathbf{b}^{\mathrm{m}} \cdot \nabla_{\boldsymbol{X}}\delta\tilde{\eta}\right)\, \mathrm{d}V - \int_{\partial\Omega^{\mathrm{mt}}_0} a^{\mathrm{mt}}\delta\tilde{\eta}\, \mathrm{d}A}_{\textbf{Micromorphic}} = 0 \tag{14}$$

Here $\mathbf{f}_0$, $\mathbf{t}_0$, and a^{mt} are the standard body force, standard traction, and generalized traction, respectively. From the comparison with the original micromorphic theory in Forest (2016), the generalized body forces in the external virtual work within micromorphic continua were ignored in this study. Additionally, lemma 1 in Eq. (14) can be rewritten.

$$\underbrace{\int_{\Omega_0} \overbrace{\left(\nabla_{\boldsymbol{X}} \cdot \mathbf{P} + \mathbf{f}_0\right)}^{\text{linear momentum}} \cdot \delta\mathbf{u}\, \mathrm{d}V - \overbrace{\int_{\partial\Omega_0} \left(\mathbf{P}\mathbf{n}_0\right) \cdot \delta\mathbf{u}\, \mathrm{d}A + \int_{\partial\Omega_0^{\mathrm{t}}} \mathbf{t}_0 \cdot \delta\mathbf{u}\, \mathrm{d}A}^{\text{standard traction}}}_{\text{Non-gradient}}$$
$$+ \underbrace{\int_{\Omega_0} \overbrace{\left(\nabla_{\boldsymbol{X}} \cdot \mathbf{b}^{\mathrm{m}} - a^{\mathrm{m}}\right)}^{\text{micromorphic balance}} \delta\tilde{\eta}\, \mathrm{d}V - \overbrace{\int_{\partial\Omega_0} \left(\mathbf{b}^{\mathrm{m}} \cdot \mathbf{n}_0\right) \delta\tilde{\eta}\, \mathrm{d}A + \int_{\partial\Omega_0^{\mathrm{mt}}} a^{\mathrm{mt}} \delta\tilde{\eta}\, \mathrm{d}A}^{\text{generalized traction}}}_{\text{Micromorphic}} = 0 \tag{15}$$

Here, the additional term $\mathbf{n}_0$ presents the normal vector with respect to the surface of reference Ω_0. Moreover, the static or quasi-static state for coupled global equilibrium can be derived with linear momentum and micromorphic extension terms, to satisfy lemma 1. The following point-wise conditions should be considered with boundary conditions.

$$\begin{cases} \underbrace{\nabla_{\boldsymbol{X}} \cdot \mathbf{P} + \mathbf{f}_0 = \mathbf{0}}_{\text{linear momentum}} & \text{within } \Omega_0; \\ \mathbf{t}_0 = \mathbf{P}\mathbf{n}_0 \quad \text{on } \partial\Omega_0^{\mathrm{t}}; \quad \mathbf{u} = \mathbf{u}^{\mathrm{given}} \quad \text{on } \partial\Omega_0^{\mathbf{u}} & \\ \underbrace{\nabla_{\boldsymbol{X}} \cdot \mathbf{b}^{\mathrm{m}} - a^{\mathrm{m}} = 0}_{\text{micromorphic balance}} & \text{within } \Omega_0; \\ a^{\mathrm{mt}} = \mathbf{b}^{\mathrm{m}} \cdot \mathbf{n}_0 \quad \text{on } \partial\Omega_0^{\mathrm{mt}}; \quad \tilde{\eta} = \tilde{\eta}^{\mathrm{given}} \quad \text{on } \partial\Omega_0^{\tilde{\eta}} & \end{cases} \tag{16}$$

The definitions contain "$\Omega_0^{\mathrm{t/mt}} \cap \Omega_0^{\mathbf{u}/\tilde{\eta}} = \emptyset$" and "$\Omega_0^{\mathrm{t/mt}} \cup \Omega_0^{\mathbf{u}/\tilde{\eta}} = \Omega_0$". Hence, notably, the microvariable that presents $\tilde{\eta}$ related to the damage hardening mechanism and is utilized to describe phenomenon of mechanism cannot be analyzed by high resolution localized characterization solely.

2.4.2. Damage modeling: local maximization of coupled dissipation

The model conclusion of the non-gradient version is shown below and is based on Eqs. (6) and (8). The damage norm can be derived.

$$Y^{\mathrm{d}} = -\left(\frac{\partial f(\mathrm{D})}{\partial \mathrm{D}} \Psi^{\mathrm{e}*} + \frac{\partial h(\mathrm{D})}{\partial \mathrm{D}} \Psi^{\mathrm{p}*}\right) \tag{17}$$

The damage criterion and the loading/unloading condition for the damage can be derived.

$$\textbf{Non-gradient} \qquad \Phi^{\mathrm{d}} = Y^{\mathrm{d}} - \beta^{\mathrm{d}} \tag{18}$$

$$\gamma_{\mathrm{d}} \geq 0, \quad \Phi^{\mathrm{d}} \leq 0, \quad \gamma_{\mathrm{d}} \Phi^{\mathrm{d}} = 0 \tag{19}$$

Applying the Lagrangian optimization $\mathcal{L}$ with the Karush–Kuhn–Tucker condition maximizes the plasticity and damage dissipations via the Lagrangian multipliers γ_{p} and γ_{d} from Eq. (6), as follows.

$$\mathcal{L} = -\left(\hat{\mathbf{M}}^{\mathrm{e}} : \mathbf{L}^{\mathrm{p}} - \tau_{\mathrm{c}} \dot{\xi} + Y^{\mathrm{d}} \dot{\mathrm{D}} - \beta^{\mathrm{d}} \dot{\eta}\right) + \gamma_{\mathrm{p}} \Phi^{\mathrm{p}} + \gamma_{\mathrm{d}} \Phi^{\mathrm{d}} \tag{20}$$

$$\begin{cases} \dfrac{\partial \mathcal{L}}{\partial \hat{\mathbf{M}}^{\mathrm{e}}} = \mathbf{0} \Rightarrow \mathbf{L}^{\mathrm{p}} = \gamma_{\mathrm{p}} \mathbf{N}^{\mathrm{p}}; & \mathbf{N}^{\mathrm{p}} = \dfrac{\partial \Phi^{\mathrm{p}}}{\partial \hat{\mathbf{M}}^{\mathrm{e}}} \\ \dot{\varepsilon}_{\mathrm{eq}}^{\mathrm{p}} = \gamma_{\mathrm{p}}; & \dfrac{\partial \mathcal{L}}{\partial \tau_{\mathrm{c}}} = 0 \Rightarrow \dot{\xi} = \gamma_{\mathrm{p}} \end{cases} \tag{21}$$

$$\begin{cases} \dfrac{\partial \mathcal{L}}{\partial Y^{\mathrm{d}}} = 0 \Rightarrow \dot{\mathrm{D}} = \gamma_{\mathrm{d}}; & \dfrac{\partial \mathcal{L}}{\partial \beta^{\mathrm{d}}} = 0 \Rightarrow \dot{\eta} = \gamma_{\mathrm{d}} \end{cases} \tag{22}$$

The effective damage variable D can be explained as an effective damage strain-like representation in the same manner as the equivalent plastic strain $\varepsilon_{\mathrm{eq}}^{\mathrm{p}}$ in the plasticity theory.

Regarding the micromorphic damage modeling, as discussed at the beginning of this section. Eq. (8) and the above operations of the non-gradient version use, the same damage norm as in Eq. (17) and the micromorphic isotropic damage hardening is obtained as follows.

$$Y^{\mathrm{d}} = -\left(\frac{\partial f(\mathrm{D})}{\partial \mathrm{D}} \Psi^{\mathrm{e}*} + \frac{\partial h(\mathrm{D})}{\partial \mathrm{D}} \Psi^{\mathrm{p}*}\right), \quad \beta^{\mathrm{m}} = \beta^{\mathrm{d}} + \frac{\partial \Psi^{\mathrm{m}}}{\partial \eta} \tag{23}$$

The damage criterion and loading/unloading condition with the micromorphic extension can be derived.

$$\textbf{Micromorphic} \qquad \Phi^{\mathrm{m}} = Y^{\mathrm{d}} - \beta^{\mathrm{m}} \tag{24}$$

$$\gamma_{\mathrm{d}} \geq 0, \quad \Phi^{\mathrm{m}} \leq 0, \quad \gamma_{\mathrm{d}} \Phi^{\mathrm{m}} = 0 \tag{25}$$

The application of Lagrangian optimization $\mathcal{L}^{\mathrm{m}}$ with the Karush–Kuhn–Tucker condition maximizes the extended dissipations,

$$\mathcal{L}^{\mathrm{m}} = -\left(\hat{\mathbf{M}}^{\mathrm{e}} : \mathbf{L}^{\mathrm{p}} - \tau_{\mathrm{c}}\dot{\xi} + Y^{\mathrm{d}}\dot{\mathrm{D}} - \beta^{\mathrm{m}}\dot{\eta}\right) + \gamma_{\mathrm{p}}\boldsymbol{\Phi}^{\mathrm{p}} + \gamma_{\mathrm{d}}\boldsymbol{\Phi}^{\mathrm{m}} \tag{26}$$

$$\begin{cases} \dfrac{\partial \mathcal{L}^{\mathrm{m}}}{\partial Y^{\mathrm{d}}} = 0 \Rightarrow \dot{\mathrm{D}} = \gamma_{\mathrm{d}}; & \dfrac{\partial \mathcal{L}^{\mathrm{m}}}{\partial \beta^{\mathrm{m}}} = 0 \Rightarrow \dot{\eta} = \gamma_{\mathrm{d}} \end{cases} \tag{27}$$

The plastic– and damage–dissipation and its optimization were not changed; however, the intrinsic evolution was changed with the micromorphic effect in β^{m}.

The damage criterion $\boldsymbol{\Phi}^{\mathrm{m}}$ can be further derived to express damage regularization via the global micromorphic balance, as shown in Eq. (16). The micromorphic damage criterion can be rewritten with Eqs. (8) and (24) and the coupling relation of the extra damage hardening term β^{e}.

$$\boldsymbol{\Phi}^{\mathrm{m}} = Y^{\mathrm{d}} - \left(\beta^{\mathrm{d}} - \nabla_{\boldsymbol{X}} \cdot \mathbf{b}^{\mathrm{m}}\right) \tag{28}$$

As explained in Note 5, the last term of the extended damage criterion is an additional source owing to the damage mechanism.

Note 5. This model can be reduced to a non-gradient version derived as shown in Eqs. (17)–(22) by disabling the a^{m}, $\mathbf{b}^{\mathrm{m}}$, and Ψ^{m} terms. The physical meaning of damage modeling with micromorphic continua was ignored in several works due to its scale transition complexity. For instance, in the comparison of Eqs. (18) and (24) for the damage criterion, the Y^{d} term should not be changed with the inclusion of micromorphic continua, as it is representative of virgin material behaviors related to specific loading conditions, such as the resolved stress norm in plasticity modeling.

2.5. Definitions of the Helmholtz free energy for constitutive relations

The constitutive modeling of not only elastoplasticity but also micromorphic damage proposed thus far is sufficiently general, although it is still dependent on different configurations. In practice, certain specific Helmholtz free energies of this model should be considered to capture different material responses. The Helmholtz free energies are defined to discuss the numerical results further and emphasize the key aspect of this study.

An undamaged compressible Neo–Hookean hyperelastic energy $\Psi^{\mathrm{e}*}$ with all quantities in the plastic intermediate configuration is chosen.

$$\Psi^{\mathrm{e}*} = \frac{\mu}{2}\left(\mathbf{C}^{\mathrm{e}} : \mathbf{1} - 3\right) - \mu \ln\left[J^{\mathrm{e}}\right] + \frac{\lambda}{2}\left(J^{\mathrm{e}}\right)^2 \tag{29}$$

Additionally, the undamaged plastic aspect $\Psi^{\mathrm{p}*}$ is chosen,

$$\Psi^{\mathrm{p}*} = \left(\tau_0 + \delta\tau_{\mathrm{s}}\right)\xi + \frac{1}{2}H^{\mathrm{p}}\xi^2 + \frac{\delta\tau_{\mathrm{s}}}{q^{\mathrm{p}}}\left(\exp\left(-q^{\mathrm{p}}\xi\right) - 1\right) \tag{30}$$

Here, the first two definitions within Eq. (8) yield the expressions of the elastic second Piola–Kirchhoff stress $\hat{\mathbf{S}}^{\mathrm{e}}$ and plastic isotropic resistance τ_{c} in the plastic intermediate configuration, as follows.

$$\hat{\mathbf{S}}^{\mathrm{e}} = f\left(\mathrm{D}\right)\hat{\mathbf{S}}^{\mathrm{e}*} = f\left(\mathrm{D}\right)\left(\mu\mathbf{1} + \left(\lambda \ln\left[J^{\mathrm{e}}\right] - \mu\right)\mathbf{C}^{\mathrm{e}-1}\right) \tag{31}$$

$$\tau_{\mathrm{c}} = h\left(\mathrm{D}\right)\tau_{\mathrm{c}}^{*} = h\left(\mathrm{D}\right)\left(\tau_0 + H^{\mathrm{p}}\xi + \delta\tau_{\mathrm{s}}\left(1 - \exp\left(-q^{\mathrm{p}}\xi\right)\right)\right) \tag{32}$$

Here, the μ and λ are the Lamé constants for the isotropic elasticity, and $J^{\mathrm{e}} = \det\left(\mathbf{F}^{\mathrm{e}}\right)$ presents the change in the volume owing to elastic deformation. According to plasticity, the mixed form with linear and voce nonlinear hardening includes the material yield strength τ_0, hardening module H^{p}, relative strength with respect to saturation $\delta\tau_{\mathrm{s}}$, and sensitivity parameter q^{p}.

However, regarding the damage aspect Ψ^{d}, a special form of non-gradient damage isotropic hardening is selected to construct the isotropic damage hardening term β^{d} in Eq. (35).

$$\Psi^{\mathrm{d}} = \Psi_0^{\mathrm{d}}\left(1 - \exp\left(-\eta\right)\right) + H^{\mathrm{d}}\left(1 - \exp\left(-\eta\right) - \eta\exp\left(-\eta\right)\right) \tag{33}$$

This term must satisfy the requirements of $\Psi^{\mathrm{d}} = 0$ and $\left(\Psi^{\mathrm{d}}\right)' = \Psi_0^{\mathrm{d}}$ when there is no damage ($\eta = 0$). Two material constants exist: the damage energy threshold Ψ_0^{d} and the damage hardening module H^{d}.

According to the micromorphic damage energy Ψ^{m}, a quadratic form of the micromorphic damage isotropic hardening is selected, and it is defined on the reference configuration via a coupling term between the isotropic η and the micromorphic damage hardening variable $\tilde{\eta}$, and gradient term $\nabla_{\boldsymbol{X}}\tilde{\eta}$.

$$\Psi^{\mathrm{m}} = \frac{1}{2}H^{\mathrm{m}}\left(\eta - \tilde{\eta}\right)^2 + \frac{1}{2}\nabla_{\boldsymbol{X}}\tilde{\eta} \cdot \boldsymbol{A} \cdot \nabla_{\boldsymbol{X}}\tilde{\eta}, \tag{34}$$

where H^{m} is the coefficient of the coupling term, and the second-order tensor $\boldsymbol{A}$ represents the general anisotropic micromorphic modulus. The definitions of the thermodynamic conjugate forces within Eq. (8) lead to the damage norm Y^{d}, damage isotropic hardening β^{d}, micromorphic damage hardening β^{e}, coupling term a^{m}, and micromorphic gradient term $\mathbf{b}^{\mathrm{m}}$ in the reference configuration, as follows:

$$\begin{cases} Y^{\mathrm{d}} = -\left(\dfrac{\partial f\left(\mathrm{D}\right)}{\partial \mathrm{D}}\Psi^{\mathrm{e}*} + \dfrac{\partial h\left(\mathrm{D}\right)}{\partial \mathrm{D}}\Psi^{\mathrm{p}*}\right) \\ \beta^{\mathrm{d}} = \exp\left(-\eta\right)\left(\Psi_0^{\mathrm{d}} + H^{\mathrm{d}}\eta\right) \\ \beta^{\mathrm{e}} = H^{\mathrm{m}}\left(\eta - \tilde{\eta}\right) \end{cases} \tag{35}$$

$$\begin{cases} a^{\mathrm{m}} = -H^{\mathrm{m}}\left(\eta - \tilde{\eta}\right) \\ \mathbf{b}^{\mathrm{m}} = \boldsymbol{A} \cdot \nabla_{\boldsymbol{X}} \tilde{\eta} \quad \underset{\text{condition}}{\overset{\text{isotropic}}{\Longrightarrow}} \quad A^{\mathrm{m}} \nabla_{\boldsymbol{X}} \tilde{\eta} \end{cases} \tag{36}$$

By assuming isotropic conditions in the gradient term, the micromorphic modulus $\boldsymbol{A}$ can be described with the scalar coefficient A^{m}. Additionally, the characteristic length can be defined as "$l_{\mathrm{c}} = \sqrt{A^{\mathrm{m}}/H^{\mathrm{m}}}$". This term expresses the transition of the microscopic damage hardening mechanism to affect the macroscopic material response in this proposed model.

However, the differences between the damage models of other works should be discussed. The $f\left(\mathrm{D}\right)$ and $h\left(\mathrm{D}\right)$ functions are the elastic and plastic stress-like degradation functions, respectively. They are not necessarily the same and are used to express different shapes of damage zones with different effective damage characterizations.

$$f\left(\mathrm{D}\right) = \exp\left(-\mathrm{D}\right), \qquad h\left(\mathrm{D}\right) = 1 - \alpha\left(1 - \exp\left(-\mathrm{D}\right)\right), \tag{37}$$

where the parameter "α" controls elastic and plastic contributions.

Note 6. Eqs. (27) and (35) conveniently formulate the direct control of the undamaged elastoplastic energy. Additionally, no bound ($\mathrm{D} \notin [0, 1]$) is shown in Fig. 1. The quadratic form of the Helmholtz free energy is reasonable for the micromorphic damage hardening. However, the material parameters H^{m} as a coupling term and A^{m} as the micromorphic modulus should differ from the damage with a bound in the microscale.

For comparison, Eqs. (18) and (24) can be expressed as follows.

$$\boldsymbol{\Phi}^{\mathrm{d}} \begin{cases} = Y^{\mathrm{d}} - \beta^{\mathrm{d}} \\ = \exp\left(-\mathrm{D}\right)\left(\Psi^{\mathrm{e}*} + \alpha\Psi^{\mathrm{p}*}\right) - \underbrace{\exp\left(-\eta\right)\left(\Psi_0^{\mathrm{d}} + H^{\mathrm{d}}\eta\right)}_{\textbf{non-gradient}} \end{cases} \tag{38}$$

$$\boldsymbol{\Phi}^{\mathrm{m}} \begin{cases} = Y^{\mathrm{d}} - \beta^{\mathrm{m}} \\ = \exp\left(-\mathrm{D}\right)\left(\Psi^{\mathrm{e}*} + \alpha\Psi^{\mathrm{p}*}\right) - \underbrace{\left(\exp\left(-\eta\right)\left(\Psi_0^{\mathrm{d}} + H^{\mathrm{d}}\eta\right) - \underline{A^{\mathrm{m}}\nabla_{\boldsymbol{X}}^2\tilde{\eta}}\right)}_{\textbf{micromorphic}} \\ = \exp\left(-\mathrm{D}\right)\left(\Psi^{\mathrm{e}*} + \alpha\Psi^{\mathrm{p}*}\right) - \underbrace{\left(\exp\left(-\eta\right)\left(\Psi_0^{\mathrm{d}} + H^{\mathrm{d}}\eta\right) + \underline{H^{\mathrm{m}}\left(\eta - \tilde{\eta}\right)}\right)}_{\textbf{micromorphic}} \end{cases} \tag{39}$$

A detailed discussion about damage criteria with specific Helmholtz free energies is presented in Notes 6 and 7. The same manner is used for the global micromorphic balance in Eq. (16), with a characteristic length of l_{c}.

$$\tilde{\eta} - l_{\mathrm{c}}^2 \nabla_{\boldsymbol{X}}^2 \tilde{\eta} = \eta, \quad \forall \boldsymbol{X} \in \Omega_0 \tag{40}$$

Finally, this term is derived as a regularized object in the proposed micromorphic extended damage model, similar to the implicit gradient model in Peerlings et al. (2001).

Note 7. The gradient-enhanced damage criterion $\boldsymbol{\Phi}^{\mathrm{m}}$ in Eq. (39) proposes ideas of damage modeling. Undamaged materials should maintain consistency in both the non-gradient and micromorphic damage cases, and this extension is considered as a type of negligible microscopic characterization. This damage modeling is explained by the additional term $\nabla_{\boldsymbol{X}}\tilde{\eta}$, which serves as a source of damage hardening β^{d}, proportional to the Laplacian of the micromorphic object $\tilde{\eta}$ from the damage hardening mechanism.

2.6. Weak form of the global nonlinear problem and its linearization

From the global linear momentum and micromorphic damage hardening balance derived in previous sections, the body force "$\mathbf{f}_0 = \mathbf{0}$" and satisfaction for "$\nabla_{\boldsymbol{X}}\tilde{\eta} \cdot \mathbf{n}_0 = 0$" are considered in Eq. (15). The weak forms of the coupled partial differential equations can be obtained by multiplying the test functions $\delta\mathbf{u}$ and $\delta\tilde{\eta}$, which must follow the related boundary constraints in Eqs. (16). Although the explanation of the weak form is brief from a mathematical variational perspective, it is beyond the scope of this study. Additionally, the weak forms can be derived from the above preliminaries and general forms expressed in Eq. (14) with the application of the principle of virtual work and definitions of constitutive relations, as follows.

$$\left\langle \mathbf{u}, \tilde{\eta}, \delta\mathbf{u} \right\rangle_{\Omega_0} = \int_{\Omega_0} \mathbf{S} : \delta\mathbf{E} \, \mathrm{d}V - \int_{\partial\Omega_0^{\mathrm{t}}} \mathbf{t}_0 \cdot \delta\mathbf{u} \, \mathrm{d}A \tag{41}$$

$$\left\langle \mathbf{u}, \tilde{\eta}, \delta\tilde{\eta} \right\rangle_{\Omega_0} = \int_{\Omega_0} H^{\mathrm{m}}\left(\eta - \tilde{\eta}\right)\delta\tilde{\eta} - A^{\mathrm{m}}\nabla_{\boldsymbol{X}}\tilde{\eta} \cdot \nabla_{\boldsymbol{X}}\delta\tilde{\eta} \, \mathrm{d}V \tag{42}$$

The "$\langle\bullet\rangle_{\Omega_0}$" here expresses the duality pairing, indicating that the variables can be defined over the domain in the reference configuration Ω_0. In general, the weak forms are geometrically and materially nonlinear. Hence, the linearization of these nonlinear equations with respect to the global nonlinear variables $\mathbf{u}$ and $\tilde{\eta}$ must be considered. The increments $\Delta\mathbf{u}$ and $\Delta\tilde{\eta}$ can be solved using a linear equation solver to achieve an iteratively converged criterion, as shown by the following linearization results with respect

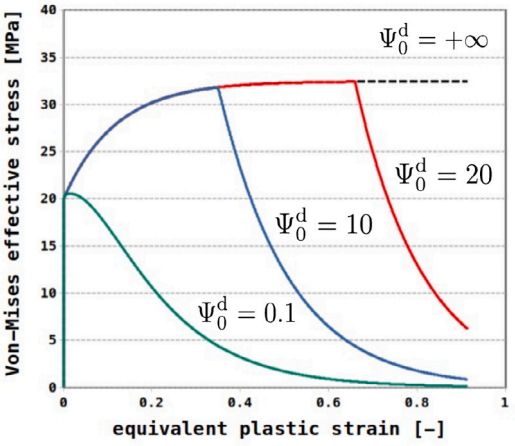

(a) Stress-strain curve

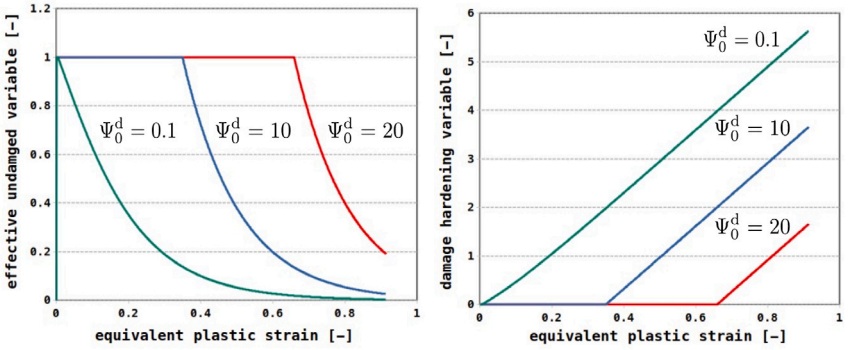

(b) Material degradation $f, h(\mathrm{D})$ (c) Damage hardening variable η

Fig. 1. Effect of the damage energy threshold Ψ_0^{d} with $H^{\mathrm{d}} = 5$; $\Psi_0^{\mathrm{d}} = 20$ in red, $\Psi_0^{\mathrm{d}} = 10$ in blue, and $\Psi_0^{\mathrm{d}} = 0.1$ in green. Pure-plasticity is shown in black dashed.

to trial variables.

$$\int_{\Omega_0} \left(\delta\mathbf{E} : \frac{\partial \mathbf{S}}{\partial \mathbf{E}} : \Delta\mathbf{E} + \nabla_{\boldsymbol{X}} \delta\mathbf{u} : \mathbf{S} \underline{\otimes} \boldsymbol{\delta} : \nabla_{\boldsymbol{X}} \Delta\mathbf{u} \right) + \delta\mathbf{E} : \frac{\partial \mathbf{S}}{\partial \tilde{\eta}} \Delta\tilde{\eta} \, \mathrm{d}V = -\left(\int_{\Omega_0} \mathbf{S} : \delta\mathbf{E} \, \mathrm{d}V - \int_{\partial\Omega_0^{\mathrm{t}}} \mathbf{t}_0 \cdot \delta\mathbf{u} \, \mathrm{d}A \right)_k \tag{43}$$

$$\int_{\Omega_0} \delta\tilde{\eta} H^{\mathrm{m}} \frac{\partial \eta}{\partial \mathbf{E}} : \Delta\mathbf{E} + \left(\delta\tilde{\eta} H^{\mathrm{m}} \left(\frac{\partial \eta}{\partial \tilde{\eta}} - 1 \right) \Delta\tilde{\eta} - A^{\mathrm{m}} \nabla_{\boldsymbol{X}} \delta\tilde{\eta} \cdot \nabla_{\boldsymbol{X}} \Delta\tilde{\eta} \right) \mathrm{d}V = -\left(\int_{\Omega_0} \delta\tilde{\eta} H^{\mathrm{m}} (\eta - \tilde{\eta}) - A^{\mathrm{m}} \nabla_{\boldsymbol{X}} \tilde{\eta} \cdot \nabla_{\boldsymbol{X}} \delta\tilde{\eta} \, \mathrm{d}V \right)_k \tag{44}$$

Here, the "$(\bullet)_k$" term represents the nonlinear residuals of the last iteration k. This formulation was based on the total Lagrangian framework over the reference configuration Ω_0 with implicit backward Euler time integration. Additionally, the standard Newton nonlinear equation and direct linear equation solver are further employed. Notably, the $\mathbf{S}$ and $\Delta\mathbf{E}$ terms are used instead of $\mathbf{P}$ and $\Delta\mathbf{F}$ terms, owing to the above having a symmetric property in accordance with vector conventions, as explained in Wriggers (2008), and Belytschko et al. (2014).

3. Implicit algorithm and material behavior

3.1. Finite element discretization

The fully coupled two–field problem modeled in the previous sections can be approximately analyzed via numerical methods. The finite element method was selected in this study due to considerations geometrical efficiency and the difficulty of obtaining analytical

solutions. The F-bar element formulation (de Souza Neto et al., 1996) was employed to avoid locking phenomena. Watanabe et al. (2008) demonstrated the effectiveness of the F-bar element in the ductile fracture analysis of periodic microstructures.

According to standard operations for finite element discretization, the analyzed domain Ω_0 can be discretized into a small, functional sub–space referred to as a continuous element and denoted Ω_0^{e}. Additionally, different types of elements have individual expressions of geometry using different order shape functions $\mathbf{N}^{\mathrm{e}}$, defined in an isoparametric space. According to Boffi et al. (2013), Oden and Demkowicz (2017), and Zienkiewicz et al. (2005), the incremental $\Delta\mathbf{u}$, $\Delta\tilde{\eta}$, and its test variables in Eqs. (43) and (44), can be discretized into elemental units and expressed by nodal components within each element.

$$\begin{aligned} &\Delta\mathbf{u} = \mathbf{N}_{\mathbf{u}}^{\mathrm{e}}\Delta\mathbf{u}^{\mathrm{e}}, \quad \delta\mathbf{u} = \mathbf{N}_{\mathbf{u}}^{\mathrm{e}}\delta\mathbf{u}^{\mathrm{e}} \\ &\Delta\tilde{\eta} = \mathbf{N}_{\tilde{\eta}}^{\mathrm{e}}\Delta\tilde{\boldsymbol{\eta}}^{\mathrm{e}}, \quad \delta\tilde{\eta} = \mathbf{N}_{\tilde{\eta}}^{\mathrm{e}}\delta\tilde{\boldsymbol{\eta}}^{\mathrm{e}} \end{aligned} \tag{45}$$

Notably, the shape functions $\mathbf{N}_{\mathbf{u}}^{\mathrm{e}}$ and $\mathbf{N}_{\tilde{\eta}}^{\mathrm{e}}$ satisfy the "inf-sup" condition to obtain solutions with a suitable order of continuity. However, the choice of discretization, such as using a different (Liebe and Steinmann, 2001; Sprave and Menzel, 2023) or the same order (Brepols et al., 2020), remains an open question. The definitions above lead to the corresponding gradient terms with respect to the undeformed configuration.

$$\begin{aligned} &\Delta\mathbf{F} = \boldsymbol{B}_{\mathbf{u}}^{\mathrm{e}}\Delta\mathbf{u}^{\mathrm{e}}, \quad \delta\mathbf{F} = \boldsymbol{B}_{\mathbf{u}}^{\mathrm{e}}\delta\mathbf{u}^{\mathrm{e}}, \\ &\Delta\mathbf{E} = \mathbf{B}_{0\mathbf{u}}^{\mathrm{e}}\Delta\mathbf{u}^{\mathrm{e}}, \quad \delta\mathbf{E} = \mathbf{B}_{0\mathbf{u}}^{\mathrm{e}}\delta\mathbf{u}^{\mathrm{e}} \\ &\nabla_{\boldsymbol{X}}\Delta\tilde{\eta} = \boldsymbol{B}_{0\tilde{\eta}}^{\mathrm{e}}\Delta\tilde{\boldsymbol{\eta}}^{\mathrm{e}}, \quad \nabla_{\boldsymbol{X}}\delta\tilde{\eta} = \boldsymbol{B}_{0\tilde{\eta}}^{\mathrm{e}}\delta\tilde{\boldsymbol{\eta}}^{\mathrm{e}} \end{aligned} \tag{46}$$

Importantly, two different formations of the displacement–strain matrix $\boldsymbol{B}^{\mathrm{e}}$ and its multiplication with the deformation gradient $\mathbf{B}_0^{\mathrm{e}}$ exist, owing to the application of incremental Green–Lagrangian strain tensor $\Delta\mathbf{E}$ in Eqs. (43) and (44), as described by de Souza Neto et al. (2011), Wriggers (2008), and Belytschko et al. (2014). Hence, the discretized formulations are shown as follows.

$$\begin{aligned} &\sum_{\mathrm{e}=1}^{\mathrm{n_e}}\delta\mathbf{u}^{\mathrm{eT}}\left\{\begin{array}{r}\left(\displaystyle\int_{\Omega_0^{\mathrm{e}}}\mathbf{B}_{0\mathbf{u}}^{\mathrm{e}}:\left[\frac{\partial\mathbf{S}}{\partial\mathbf{E}}\right]^{\mathrm{e}}:\mathbf{B}_{0\mathbf{u}}^{\mathrm{e}}+\boldsymbol{B}_{\mathbf{u}}^{\mathrm{e}}:\mathrm{S}_{jl}\delta_{ik}:\boldsymbol{B}_{\mathbf{u}}^{\mathrm{e}}\,\mathrm{d}V\right)\Delta\mathbf{u}^{\mathrm{e}}\\ +\displaystyle\int_{\Omega_0^{\mathrm{e}}}\mathbf{B}_{0\mathbf{u}}^{\mathrm{e}}:\left[\frac{\partial\mathbf{S}}{\partial\tilde{\eta}}\right]^{\mathrm{e}}\cdot\mathbf{N}_{\tilde{\eta}}^{\mathrm{e}}\,\mathrm{d}V\Delta\tilde{\boldsymbol{\eta}}^{\mathrm{e}}\end{array}\right\}\\ &\quad=-\sum_{\mathrm{e}=1}^{\mathrm{n_e}}\delta\mathbf{u}^{\mathrm{eT}}\left\{\left(\int_{\Omega_0^{\mathrm{e}}}\mathbf{B}_{0\mathbf{u}}^{\mathrm{e}}:[\mathbf{S}]^{\mathrm{e}}\,\mathrm{d}V-\int_{\partial\Omega_0^{\mathrm{te}}}\mathbf{N}_{\mathbf{u}}^{\mathrm{e}}\cdot\mathbf{t}_0\,\mathrm{d}A\right)_k\right\} \end{aligned} \tag{47}$$

$$\begin{aligned} &\sum_{\mathrm{e}=1}^{\mathrm{n_e}}\delta\tilde{\boldsymbol{\eta}}^{\mathrm{eT}}\left\{\begin{array}{r}\displaystyle\int_{\Omega_0^{\mathrm{e}}}\mathbf{N}_{\tilde{\eta}}^{\mathrm{e}}\cdot\left[H^{\mathrm{m}}\frac{\partial\eta}{\partial\mathbf{E}}\right]^{\mathrm{e}}:\mathbf{B}_{0\mathbf{u}}^{\mathrm{e}}\,\mathrm{d}V\Delta\mathbf{u}^{\mathrm{e}}+\\ \displaystyle\int_{\Omega_0^{\mathrm{e}}}\mathbf{N}_{\tilde{\eta}}^{\mathrm{e}}\cdot\left[H^{\mathrm{m}}\left(\frac{\partial\eta}{\partial\tilde{\eta}}-1\right)\right]^{\mathrm{e}}\mathbf{N}_{\tilde{\eta}}^{\mathrm{e}}-\left[A^{\mathrm{m}}\right]^{\mathrm{e}}\boldsymbol{B}_{0\tilde{\eta}}^{\mathrm{e}}\cdot\boldsymbol{B}_{0\tilde{\eta}}^{\mathrm{e}}\,\mathrm{d}V\Delta\tilde{\boldsymbol{\eta}}^{\mathrm{e}}\end{array}\right\}\\ &=-\sum_{\mathrm{e}=1}^{\mathrm{n_e}}\delta\tilde{\boldsymbol{\eta}}^{\mathrm{eT}}\left\{\left(\int_{\Omega_0^{\mathrm{e}}}\mathbf{N}_{\tilde{\eta}}^{\mathrm{e}}\cdot\left[H^{\mathrm{m}}(\eta-\tilde{\eta})\right]^{\mathrm{e}}-\boldsymbol{B}_{0\tilde{\eta}}^{\mathrm{e}}\cdot\left[A^{\mathrm{m}}\nabla_{\boldsymbol{X}}\delta\tilde{\eta}\right]^{\mathrm{e}}\,\mathrm{d}V\right)_k\right\} \end{aligned} \tag{48}$$

To avoid the volumetric locking that occurs during localization due to damage, $\bar{\mathbf{F}}$ averaging of the volumetric deformation gradient over each element was used to calculate the stress state and construct only $\mathbf{B}_0^{\mathrm{e}}$ in the Jacobian terms instead of the standard deformation gradient $\mathbf{F}$ (de Souza Neto et al., 1996). The discretized equations can be written in elemental form using certain quadrature rules.

$$\left(\begin{bmatrix}\boldsymbol{k}_{\mathbf{uu}} & \boldsymbol{k}_{\mathbf{u}\tilde{\eta}}\\ \boldsymbol{k}_{\tilde{\eta}\mathbf{u}} & \boldsymbol{k}_{\tilde{\eta}\tilde{\eta}}\end{bmatrix}^{\mathrm{e}}\begin{Bmatrix}\Delta\mathbf{u}\\ \Delta\tilde{\boldsymbol{\eta}}\end{Bmatrix}^{\mathrm{e}}\right)_{k+1}=-\left(\begin{Bmatrix}\boldsymbol{r}_{\mathbf{u}}\\ \boldsymbol{r}_{\tilde{\eta}}\end{Bmatrix}^{\mathrm{e}}\right)_k \tag{49}$$

$$\left([\boldsymbol{K}]\{\Delta\boldsymbol{d}\}\right)_{k+1}=-\left(\{\boldsymbol{R}_{\boldsymbol{d}}\}\right)_k \tag{50}$$

The global linearized Eq. (50) can be constructed by standard finite element assembly operations "$\mathcal{A}(\bullet)$" on elemental candidates in Eq. (49). The above equations are general, as the different material responses within the same coupled problem can separately focus on the consistent tangent matrices (CTM) on each quadrature point within the integration method as shown below.

$$\begin{aligned} [\boldsymbol{J}]^{\mathrm{CTM/e}} &= \begin{bmatrix}\boldsymbol{J}_{\mathbf{uu}} & \boldsymbol{J}_{\mathbf{u}\tilde{\eta}}\\ \boldsymbol{J}_{\tilde{\eta}\mathbf{u}} & \boldsymbol{J}_{\tilde{\eta}\tilde{\eta}}\end{bmatrix}^{\mathrm{e}} \quad \textbf{extra from} \quad \begin{bmatrix}\boldsymbol{k}_{\mathbf{uu}} & \boldsymbol{k}_{\mathbf{u}\tilde{\eta}}\\ \boldsymbol{k}_{\tilde{\eta}\mathbf{u}} & \boldsymbol{k}_{\tilde{\eta}\tilde{\eta}}\end{bmatrix}^{\mathrm{e}}\\ &=\begin{bmatrix}\underbrace{\left[\frac{\partial\mathbf{S}}{\partial\mathbf{E}}\right]}_{\boldsymbol{J}_{\mathbf{uu}}} & \underbrace{\left[\frac{\partial\mathbf{S}}{\partial\tilde{\eta}}\quad\frac{\partial\mathbf{S}}{\partial\nabla_{\boldsymbol{X}}\tilde{\eta}}\right]}_{\boldsymbol{J}_{\mathbf{u}\tilde{\eta}}}\\ \underbrace{\begin{bmatrix}H^{\mathrm{m}}\frac{\partial\eta}{\partial\mathbf{E}}\\ \frac{\partial\mathbf{b}^{\mathrm{m}}}{\partial\mathbf{E}}\end{bmatrix}}_{\boldsymbol{J}_{\tilde{\eta}\mathbf{u}}} & \underbrace{\begin{bmatrix}H^{\mathrm{m}}\left(\frac{\partial\eta}{\partial\tilde{\eta}}-1\right) & 0\\ 0 & A^{\mathrm{m}}\end{bmatrix}}_{\boldsymbol{J}_{\tilde{\eta}\tilde{\eta}}}\end{bmatrix}^{\mathrm{e}} \end{aligned} \tag{51}$$

This procedure is also called an operation at the material-point level. CTMs should correspond to certain stress-update algorithms and correct the configuration–transformation. Additionally, each component of the CTMs "$[\boldsymbol{J}]$" is calculated in Section 3.3.

3.2. Evolution equations and stress update algorithm

As described in Section 2.3 regarding plasticity and Section 3.1 regarding the CTM, the implicit time integration for plasticity and damage via the general exponential mapping on the plastic intermediate configuration and the scalar Euler backward algorithm, respectively, were used.

Eq. (21) for the plastic flow rule yields the following,

$$\dot{\mathbf{F}}^{\mathrm{p}} = \gamma_{\mathrm{p}} \mathbf{N}^{\mathrm{p}} \mathbf{F}^{\mathrm{p}} \tag{52}$$

The application of implicit exponential mapping and incremental Lagrangian multiplier $\left(\Delta\gamma_{\mathrm{p}}\right)_{\mathrm{n+1}} = \Delta t \gamma_{\mathrm{p}} = \left(t_{\mathrm{n+1}} - t_n\right)\gamma_{\mathrm{p}}$ yields the following.

$$\mathbf{F}^{\mathrm{p}}_{\mathrm{n+1}} = \exp\left(\left(\Delta\gamma_{\mathrm{p}}\right)_{\mathrm{n+1}} \mathbf{N}^{\mathrm{p}}\right)\mathbf{F}^{\mathrm{p}}_{\mathrm{n}}; \quad \mathbf{F}^{\mathrm{e}}_{\mathrm{n+1}} = \mathbf{F}^{\mathrm{e/trial}}_{\mathrm{n+1}} \exp\left(-\left(\Delta\gamma_{\mathrm{p}}\right)_{\mathrm{n+1}} \mathbf{N}^{\mathrm{p}}\right) \tag{53}$$

However, for scalar Euler backward time integration, the evolution of the effective damage variable D and strain-like internal state variables, such as the isotropic plastic hardening ξ and, isotropic damage hardening η are derived from Eqs. (21) and (27) as follows.

$$\begin{cases} \xi_{\mathrm{n+1}} = \xi_{\mathrm{n}} + \left(\Delta\gamma_{\mathrm{p}}\right)_{\mathrm{n+1}} \\ \eta_{\mathrm{n+1}} = \eta_{\mathrm{n}} + \left(\Delta\gamma_{\mathrm{d}}\right)_{\mathrm{n+1}} \\ \mathrm{D}_{\mathrm{n+1}} = \mathrm{D}_{\mathrm{n}} + \left(\Delta\gamma_{\mathrm{d}}\right)_{\mathrm{n+1}} \end{cases} \tag{54}$$

The difference between the continuum material Jacobian and consistent (or algorithmic) material Jacobian can be eliminated via the application of exponential mapping for plasticity (Terada and Watanabe, 2007). The stress-update algorithm is presented below to discuss the implementation of the model.

To mimic the implementation in strain-rate-independent single crystal plasticity (Watanabe et al., 2005), potential active set searching is used to determine the current loading conditions, including undamaged elasticity, damaged elasticity, undamaged elastoplasticity, and damaged elastoplasticity, as emphasized in Note 1. This relates to two trial criteria for plasticity and damage.

$$\boldsymbol{\Phi}^{\mathrm{p/trial}} = f(\mathrm{D})_{\mathrm{n}} |\tau^*_{\mathrm{r}}|^{\mathrm{trial}}_{\mathrm{n+1}} - h(\mathrm{D})_{\mathrm{n}} \left(\tau^*_{\mathrm{c}}\right)_{\mathrm{n}} \tag{55}$$

$$\boldsymbol{\Phi}^{\mathrm{m/trial}} = Y^{\mathrm{d/trial}}_{\mathrm{n+1}} - \left(\left(\beta^{\mathrm{d}}\right)_{\mathrm{n}} + \left(\beta^{\mathrm{e}}\right)^{\mathrm{trial}}_{\mathrm{n+1}}\right) \tag{56}$$

The known values include $\mathbf{F}_{\mathrm{n+1}}$, $\tilde{\eta}_{\mathrm{n+1}}$, $\nabla_{\boldsymbol{X}}\tilde{\eta}_{\mathrm{n+1}}$, $\mathbf{F}_{\mathrm{n}}$, $\mathbf{F}^{\mathrm{e}}_{\mathrm{n}}$, ξ_{n}, η_{n}, and D_{n}. Trial values can be obtained to judge the current loading condition.

The trial elastic resultants from Eqs. (1), (8), and (31) follow.

$$\mathbf{F}^{\mathrm{e/trial}}_{\mathrm{n+1}} = \mathbf{F}_{\mathrm{n+1}}\mathbf{F}^{-1}_{\mathrm{n}}\mathbf{F}^{\mathrm{e}}_{\mathrm{n}}, \quad \mathbf{C}^{\mathrm{e/trial}}_{\mathrm{n+1}} = \mathbf{F}^{\mathrm{e/trialT}}_{\mathrm{n+1}}\mathbf{F}^{\mathrm{e/trial}}_{\mathrm{n+1}} \tag{57}$$

$$\hat{\mathbf{S}}^{\mathrm{e*/trial}}_{\mathrm{n+1}} = \mu\mathbf{1} + \left(\lambda \ln\left[J^{\mathrm{e/trial}}_{\mathrm{n+1}}\right] - \mu\right)\mathbf{C}^{\mathrm{e/trial-1}}_{\mathrm{n+1}} \tag{58}$$

$$\hat{\mathbf{M}}^{\mathrm{e*/trial}}_{\mathrm{n+1}} = \mathbf{C}^{\mathrm{e/trial}}_{\mathrm{n+1}}\hat{\mathbf{S}}^{\mathrm{e*/trial}}_{\mathrm{n+1}} \tag{59}$$

The trial resultants of the plasticity and damage criteria, and plastic flow tensor follow.

$$|\tau^*_{\mathrm{r}}|^{\mathrm{trial}}_{\mathrm{n+1}} = \sqrt{\frac{3}{2}}\sqrt{\mathrm{dev}\left(\hat{\mathbf{M}}^{\mathrm{e*/trial}}_{\mathrm{n+1}}\right) : \mathrm{dev}\left(\hat{\mathbf{M}}^{\mathrm{e*/trial}}_{\mathrm{n+1}}\right)^{\mathrm{T}}} \tag{60}$$

$$Y^{\mathrm{d/trial}}_{\mathrm{n+1}} = \exp\left(-\mathrm{D}_{\mathrm{n}}\right)\left(\boldsymbol{\Psi}^{\mathrm{e*/trial}}_{\mathrm{n+1}} + \alpha\boldsymbol{\Psi}^{\mathrm{p*}}_{\mathrm{n}}\right) \tag{61}$$

$$\mathbf{N}^{\mathrm{p}}_{\mathrm{n+1}} = \frac{3}{2}\frac{\mathrm{dev}\left(\hat{\mathbf{M}}^{\mathrm{e*/trial}}_{\mathrm{n+1}}\right)^{\mathrm{T}}}{\left(\tau^*_{\mathrm{r}}\right)^{\mathrm{trial}}_{\mathrm{n+1}}} \tag{62}$$

Here, the trial resolved stress norm $|\tau^*_{\mathrm{r}}|$ and trial damaged norm Y^{d} are variants with the loading condition. They should be dependent on the materials but the microscopic mechanisms are emphasized in Notes 5 and 7.

Following the current active set, the most complicated case (ductile fracture) is presented. Nonlinear equations at the material-point level should be solved iteratively to identify the correct increments of the Lagrangian multipliers $\left(\Delta\gamma_{\mathrm{p}}\right)_{\mathrm{n+1}}$ and $\left(\Delta\gamma_{\mathrm{d}}\right)_{\mathrm{n+1}}$. The linearization of the interior nonlinear Equations (20) and (39) for Newton iteration follow.

$$\left(\begin{bmatrix} \frac{\mathrm{d}\boldsymbol{\Phi}^{\mathrm{p}}}{\mathrm{d}\Delta\gamma_{\mathrm{p}}} & \frac{\mathrm{d}\boldsymbol{\Phi}^{\mathrm{p}}}{\mathrm{d}\Delta\gamma_{\mathrm{d}}} \\ \frac{\mathrm{d}\boldsymbol{\Phi}^{\mathrm{m}}}{\mathrm{d}\Delta\gamma_{\mathrm{p}}} & \frac{\mathrm{d}\boldsymbol{\Phi}^{\mathrm{m}}}{\mathrm{d}\Delta\gamma_{\mathrm{d}}} \end{bmatrix}\begin{Bmatrix} \Delta\left(\Delta\gamma_{\mathrm{p}}\right) \\ \Delta\left(\Delta\gamma_{\mathrm{d}}\right) \end{Bmatrix}_{\mathrm{n+1}}\right)_{k+1} = -\left(\begin{Bmatrix} \boldsymbol{\Phi}^{\mathrm{p}} \\ \boldsymbol{\Phi}^{\mathrm{m}} \end{Bmatrix}_{\mathrm{n+1}}\right)_{k} \tag{63}$$

$$\begin{cases} \left(\left(\Delta\gamma_{\mathrm{p}}\right)_{\mathrm{n+1}}\right)_{k+1} = \left(\left(\Delta\gamma_{\mathrm{p}}\right)_{\mathrm{n+1}}\right)_{k} + \left(\Delta\left(\Delta\gamma_{\mathrm{p}}\right)_{\mathrm{n+1}}\right)_{k+1} \\ \left(\left(\Delta\gamma_{\mathrm{d}}\right)_{\mathrm{n+1}}\right)_{k+1} = \left(\left(\Delta\gamma_{\mathrm{d}}\right)_{\mathrm{n+1}}\right)_{k} + \left(\Delta\left(\Delta\gamma_{\mathrm{d}}\right)_{\mathrm{n+1}}\right)_{k+1} \end{cases} \tag{64}$$

When the above nonlinear equation converges, the evolution and correct stress-like the resultants $\hat{\mathbf{S}}^{\mathrm{e}}_{\mathrm{n+1}}$, $f\left(\mathrm{D}_{\mathrm{n+1}}\right)$, and $h\left(\mathrm{D}_{\mathrm{n+1}}\right)$ can be calculated by $\mathbf{F}^{\mathrm{e}}_{\mathrm{n+1}}$ and $\mathrm{D}_{\mathrm{n+1}}$ from Eqs. (31), (37), (53), and (54). Additionally, some pullback/pushforward of covariant and contravariant second-order tensors are used for the finite element analysis in Section 3.1.

3.3. Consistent tangent matrix

After the converged results of the nonlinear equation at the material-point level, all internal variables can be correctly updated. Simultaneously, Eq. (51) should be followed, and the consistent tangent matrices should be provided for the global nonlinear equation solver in the implicit finite element analysis. These algorithms are shown below.

The relation between $\Delta\mathbf{S}_{n+1}$ with $\Delta\mathbf{E}_{n+1}$ and $\Delta\tilde{\eta}_{n+1}$ follows:

$$\Delta\mathbf{S}_{n+1} = \frac{\partial\mathbf{S}}{\partial\mathbf{E}} : \Delta\mathbf{E}_{n+1} + \frac{\partial\mathbf{S}}{\partial\tilde{\eta}}\Delta\tilde{\eta}_{n+1} \tag{65}$$

The variation within the first term can be extended from the previous finite strain elastoplastic "non-gradient" damage model (Watanabe et al., 2008). Its only difference from the micromorphic damage model is the expression of the damage criterion and evolution via certain regularization. Regarding the plastic aspect in the intermediate configuration, the conclusion of the consistent tangent matrix related to the second Piola–Kirchhoff stress with the Green–Lagrangian strain tensor follows:

The application of the Oldroyd-type material rate $\mathscr{L}^{\mathrm{p}}_{\Delta\mathbf{u}}$ correctly expresses the transformation from the plastic intermediate configuration to the reference configuration, as shown in Eq. (65). The contravariant second-order tensor, such as the stress tensor, follows.

$$\begin{aligned}\Delta\mathbf{S} &= \Delta\left[\mathbf{F}^{\mathrm{p}-1}\hat{\mathbf{S}}^{\mathrm{e}}\mathbf{F}^{\mathrm{p}-\mathrm{T}}\right]\\ &= \Delta\mathbf{F}^{\mathrm{p}-1}\hat{\mathbf{S}}^{\mathrm{e}}\mathbf{F}^{\mathrm{p}-\mathrm{T}} + \mathbf{F}^{\mathrm{p}-1}\hat{\mathbf{S}}^{\mathrm{e}}\Delta\mathbf{F}^{\mathrm{p}-\mathrm{T}} + \mathbf{F}^{\mathrm{p}-1}\Delta\hat{\mathbf{S}}^{\mathrm{e}}\mathbf{F}^{\mathrm{p}-\mathrm{T}}\end{aligned} \tag{66}$$

$$\begin{aligned}&\Delta\mathbf{S}^{\mathrm{p}} = \mathbf{F}^{\mathrm{p}}\Delta\mathbf{S}\mathbf{F}^{\mathrm{p}\mathrm{T}}\\ &\textbf{define}: \quad \mathscr{L}^{\mathrm{p/contra}}_{\Delta\mathbf{u}}\left(\hat{\mathbf{S}}^{\mathrm{e}}\right) = \Delta\mathbf{S}^{\mathrm{p}}\end{aligned} \tag{67}$$

Additionally, the covariant second-order tensor, such as the strain tensor, from the plastic intermediate configuration follows.

$$\begin{aligned}\Delta\mathbf{E} &= \Delta\left[\mathbf{F}^{\mathrm{p}\mathrm{T}}\mathbf{E}^{\mathrm{e}}\mathbf{F}^{\mathrm{p}}\right]\\ &= \Delta\mathbf{F}^{\mathrm{p}\mathrm{T}}\mathbf{E}^{\mathrm{e}}\mathbf{F}^{\mathrm{p}} + \mathbf{F}^{\mathrm{p}\mathrm{T}}\mathbf{E}^{\mathrm{e}}\Delta\mathbf{F}^{\mathrm{p}} + \mathbf{F}^{\mathrm{p}\mathrm{T}}\Delta\mathbf{E}^{\mathrm{e}}\mathbf{F}^{\mathrm{p}}\end{aligned} \tag{68}$$

$$\begin{aligned}&\Delta\mathbf{E}^{\mathrm{p}} = \mathbf{F}^{\mathrm{p}-\mathrm{T}}\Delta\mathbf{E}\mathbf{F}^{\mathrm{p}-1}\\ &\textbf{define}: \quad \mathscr{L}^{\mathrm{p/co}}_{\Delta\mathbf{u}}\left(\mathbf{E}^{\mathrm{e}}\right) = \Delta\mathbf{E}^{\mathrm{p}}\end{aligned} \tag{69}$$

With these above definitions of the material rate, the elastoplastic damage consistent tangent matrix $\bar{\mathbb{C}}^{\mathrm{epd}}$ on the reference configuration can be expressed via the term $\hat{\mathbb{C}}^{\mathrm{epd}}$ on the plastic intermediate configuration follows.

$$\begin{aligned}&\mathscr{L}^{\mathrm{p/contra}}_{\Delta\mathbf{u}}\left(\hat{\mathbf{S}}^{\mathrm{e}}\right) = \hat{\mathbb{C}}^{\mathrm{epd}} : \mathscr{L}^{\mathrm{p/co}}_{\Delta\mathbf{u}}\left(\mathbf{E}^{\mathrm{e}}\right) + \hat{\mathbb{D}}^{\mathrm{S}\tilde{\eta}}\Delta\tilde{\eta}\\ &\frac{\partial\mathbf{S}}{\partial\mathbf{E}} = \bar{\mathbb{C}}^{\mathrm{epd}}_{IJKL} = \mathrm{F}^{\mathrm{p}-1}_{Ia}\mathrm{F}^{\mathrm{p}-1}_{Jb}\mathrm{F}^{\mathrm{p}-1}_{Kc}\mathrm{F}^{\mathrm{p}-1}_{Ld}\hat{\mathbb{C}}^{\mathrm{epd}}_{abcd}\\ &\frac{\partial\mathbf{S}}{\partial\tilde{\eta}} = \mathrm{F}^{\mathrm{p}-1}_{Ia}\hat{\mathbb{D}}^{\mathrm{S}\tilde{\eta}}_{ab}\mathrm{F}^{\mathrm{p}-\mathrm{T}}_{bJ}\end{aligned} \tag{70}$$

The second term of Eq. (65) can be naturally obtained via $\hat{\mathbb{D}}^{\mathrm{S}\tilde{\eta}}$. According to the above truth in the case of fully coupled plasticity damaging, the variation of incremental plastic deformation gradient $\Delta\mathbf{F}^{\mathrm{p}}_{n+1}$ is derived.

$$\Delta\mathbf{F}^{\mathrm{p}}_{n+1} = \frac{\partial\mathbf{F}^{\mathrm{p}}}{\partial\mathbf{E}^{\mathrm{e}}} : \Delta\mathbf{E}^{\mathrm{e}}_{n+1} + \frac{\partial\mathbf{F}^{\mathrm{p}}}{\partial\tilde{\eta}}\Delta\tilde{\eta}_{n+1} \tag{71}$$

The incremental effective damage variable $\Delta\mathrm{D}_{n+1}$ implicitly depends on the plastic and micromorphic damage hardening contributions shown in Eq. (54). Additionally, the variation of the elastic Piola–Kirchhoff stress $\Delta\hat{\mathbf{S}}^{\mathrm{e}}_{n+1}$ can be expressed by Eq. (31) as well as Eq. (70).

$$\Delta\hat{\mathbf{S}}^{\mathrm{e}}_{n+1} = \frac{\partial\hat{\mathbf{S}}^{\mathrm{e}}}{\partial\mathbf{E}^{\mathrm{e}}} : \Delta\mathbf{E}^{\mathrm{e}}_{n+1} + \frac{\partial\hat{\mathbf{S}}^{\mathrm{e}}}{\partial\mathrm{D}}\Delta\mathrm{D}_{n+1} \tag{72}$$

$$\Delta\mathrm{D}_{n+1} = \frac{\partial\mathrm{D}}{\partial\Delta\gamma_{\mathrm{d}}}\Delta\left(\Delta\gamma_{\mathrm{d}}\right)_{n+1} \tag{73}$$

The above variations with respect to plasticity and damage only depend on the converged $\Delta\left(\Delta\gamma_{\mathrm{p}}\right)_{n+1}$ and $\Delta\left(\Delta\gamma_{\mathrm{d}}\right)_{n+1}$ in the stress-update algorithm. Hence, the application of consistent conditions in Eqs. (12) and (25) is used to find the variation of the above Lagrangian multipliers.

$$\begin{aligned}\Delta\Phi^{\mathrm{p}} &= \frac{\partial\Phi^{\mathrm{p}}}{\partial\mathbf{E}^{\mathrm{e}}} : \Delta\mathbf{E}^{\mathrm{e}} + \frac{\partial\Phi^{\mathrm{p}}}{\partial\Delta\gamma_{\mathrm{p}}}\Delta\left(\Delta\gamma_{\mathrm{p}}\right) + \frac{\partial\Phi^{\mathrm{p}}}{\partial\Delta\gamma_{\mathrm{d}}}\Delta\left(\Delta\gamma_{\mathrm{d}}\right) + \frac{\partial\Phi^{\mathrm{p}}}{\partial\tilde{\eta}}\Delta\tilde{\eta} \quad &= 0\\ \Delta\Phi^{\mathrm{m}} &= \frac{\partial\Phi^{\mathrm{m}}}{\partial\mathbf{E}^{\mathrm{e}}} : \Delta\mathbf{E}^{\mathrm{e}} + \frac{\partial\Phi^{\mathrm{m}}}{\partial\Delta\gamma_{\mathrm{p}}}\Delta\left(\Delta\gamma_{\mathrm{p}}\right) + \frac{\partial\Phi^{\mathrm{m}}}{\partial\Delta\gamma_{\mathrm{d}}}\Delta\left(\Delta\gamma_{\mathrm{d}}\right) + \frac{\partial\Phi^{\mathrm{m}}}{\partial\tilde{\eta}}\Delta\tilde{\eta} \quad &= 0\end{aligned} \tag{74}$$

With the application of Eqs. (68) and (69) replacing $\Delta\mathbf{E}^{\mathrm{e}}$, the expressions of $\Delta\left(\Delta\gamma_{\mathrm{p}}\right)_{n+1}$ and $\Delta\left(\Delta\gamma_{\mathrm{d}}\right)_{n+1}$ can be changed as follows.

$$\begin{Bmatrix}\Delta\left(\Delta\gamma_{\mathrm{p}}\right)\\ \Delta\left(\Delta\gamma_{\mathrm{d}}\right)\end{Bmatrix}_{n+1} = -\begin{bmatrix}\frac{\mathrm{d}\Phi^{\mathrm{p}}}{\mathrm{d}\Delta\gamma_{\mathrm{p}}} & \frac{\mathrm{d}\Phi^{\mathrm{p}}}{\mathrm{d}\Delta\gamma_{\mathrm{d}}}\\ \frac{\mathrm{d}\Phi^{\mathrm{m}}}{\mathrm{d}\Delta\gamma_{\mathrm{p}}} & \frac{\mathrm{d}\Phi^{\mathrm{m}}}{\mathrm{d}\Delta\gamma_{\mathrm{d}}}\end{bmatrix}^{-1}\begin{Bmatrix}\frac{\partial\Phi^{\mathrm{p}}}{\partial\mathbf{E}^{\mathrm{e}}} : \mathscr{L}^{\mathrm{p/co}}_{\Delta\mathbf{u}}\left(\mathbf{E}^{\mathrm{e}}\right) + \frac{\partial\Phi^{\mathrm{p}}}{\partial\tilde{\eta}}\Delta\tilde{\eta}\\ \frac{\partial\Phi^{\mathrm{m}}}{\partial\mathbf{E}^{\mathrm{e}}} : \mathscr{L}^{\mathrm{p/co}}_{\Delta\mathbf{u}}\left(\mathbf{E}^{\mathrm{e}}\right) + \frac{\partial\Phi^{\mathrm{m}}}{\partial\tilde{\eta}}\Delta\tilde{\eta}\end{Bmatrix} \tag{75}$$

The first term contains the Jacobians of the interior nonlinear Equations (63) at the converged state and the results in Eqs. (66) and (67). Next, these results are used to replace values $\Delta\left(\Delta\gamma_{\mathrm{p}}\right)_{\mathrm{n+1}}$ and $\Delta\left(\Delta\gamma_{\mathrm{d}}\right)_{\mathrm{n+1}}$, with Eqs. (70) leading to $\hat{\mathbb{C}}^{\mathrm{epd}}_{abcd}$ and $\hat{\mathbb{D}}^{\mathrm{S}\eta}_{ab}$ being the primary diagonal/off-diagonal consistent tangent Jacobians within the linear momentum equilibrium.

The relation between $\Delta a^{\mathrm{m}}_{\mathrm{n+1}}$ with $\Delta\mathbf{E}_{\mathrm{n+1}}$ and $\Delta\tilde{\eta}_{\mathrm{n+1}}$ follows.

$$\Delta a^{\mathrm{m}}_{\mathrm{n+1}} = \frac{\partial a^{\mathrm{m}}}{\partial \mathbf{E}} : \Delta\mathbf{E}_{\mathrm{n+1}} + \frac{\partial a^{\mathrm{m}}}{\partial \tilde{\eta}}\Delta\tilde{\eta}_{\mathrm{n+1}} \tag{76}$$

Here, the incremental coupled micromorphic force $\Delta a^{\mathrm{m}}_{\mathrm{n+1}}$ still only depends on $\Delta\left(\Delta\gamma_{\mathrm{p}}\right)_{\mathrm{n+1}}$ and $\Delta\left(\Delta\gamma_{\mathrm{d}}\right)_{\mathrm{n+1}}$. Additionally, the constitutive relation in Eq. (36) can be used, and rewritten as shown below.

$$\Delta a^{\mathrm{m}}_{\mathrm{n+1}} = H^{\mathrm{m}}\frac{\partial \eta}{\partial \mathbf{E}} : \Delta\mathbf{E}_{\mathrm{n+1}} + H^{\mathrm{m}}\left(\frac{\partial \eta}{\partial \tilde{\eta}} - 1\right)\Delta\tilde{\eta}_{\mathrm{n+1}} \tag{77}$$

The same operation used for the second diagonal/off-diagonal consistent tangent Jacobians within the micromorphic global balance follows.

$$\begin{aligned}
\Delta a^{\mathrm{m}}_{\mathrm{n+1}} &= H^{\mathrm{m}}\bar{\mathbb{A}}^{\eta\mathrm{E}} : \mathscr{L}^{\mathrm{p/co}}_{\Delta\mathbf{u}}\left(\mathbf{E}^{\mathrm{e}}\right) + H^{\mathrm{m}}\left(\hat{\mathbb{D}}^{\eta\tilde{\eta}} - 1\right)\Delta\tilde{\eta} \\
\frac{\partial \eta}{\partial \mathbf{E}} &= \bar{\mathbb{A}}^{\eta\mathrm{E}}_{IJ} = \mathrm{F}^{\mathrm{p}-1}_{Ia}\hat{\mathbb{A}}^{\eta\mathrm{E}}_{ab}\mathrm{F}^{\mathrm{p}-\mathrm{T}}_{bJ} \\
\frac{\partial \eta}{\partial \tilde{\eta}} &= \hat{\mathbb{D}}^{\eta\tilde{\eta}}
\end{aligned} \tag{78}$$

From Eq. (54), regarding the evolution of the damage hardening variable at the material-point level and Eq. (75), the above consistent tangent components can be derived.

$$\begin{aligned}
\Delta\eta_{\mathrm{n+1}} &= \frac{\partial \eta}{\partial \Delta\gamma_{\mathrm{d}}}\Delta\left(\Delta\gamma_{\mathrm{d}}\right)_{\mathrm{n+1}} \\
&= -\frac{\partial \eta}{\partial \Delta\gamma_{\mathrm{d}}}\begin{bmatrix}\frac{\mathrm{d}\Phi^{\mathrm{m}}}{\mathrm{d}\Delta\gamma_{\mathrm{p}}} & \frac{\mathrm{d}\Phi^{\mathrm{m}}}{\mathrm{d}\Delta\gamma_{\mathrm{d}}}\end{bmatrix}^{-1}\begin{Bmatrix}\frac{\partial \Phi^{\mathrm{p}}}{\partial \mathbf{E}^{\mathrm{e}}} : \mathscr{L}^{\mathrm{p/co}}_{\Delta\mathbf{u}}\left(\mathbf{E}^{\mathrm{e}}\right) + \frac{\partial \Phi^{\mathrm{p}}}{\partial \tilde{\eta}}\Delta\tilde{\eta} \\ \frac{\partial \Phi^{\mathrm{m}}}{\partial \mathbf{E}^{\mathrm{e}}} : \mathscr{L}^{\mathrm{p/co}}_{\Delta\mathbf{u}}\left(\mathbf{E}^{\mathrm{e}}\right) + \frac{\partial \Phi^{\mathrm{m}}}{\partial \tilde{\eta}}\Delta\tilde{\eta}\end{Bmatrix}
\end{aligned} \tag{79}$$

After the pullback in Eq. (78), the results for the second diagonal/off-diagonal consistent tangent Jacobians within the micromorphic global balance can be obtained.

The relation between $\Delta\mathbf{b}^{\mathrm{m}}_{\mathrm{n+1}}$ with $\nabla_{\boldsymbol{X}}\Delta\tilde{\eta}_{\mathrm{n+1}}$ follows.

$$\Delta\mathbf{b}^{\mathrm{m}}_{\mathrm{n+1}} = \frac{\partial \mathbf{b}^{\mathrm{m}}}{\partial \nabla_{\boldsymbol{X}}\tilde{\eta}} \cdot \nabla_{\boldsymbol{X}}\Delta\tilde{\eta}_{\mathrm{n+1}} \tag{80}$$

The above term represents a relatively general case related to the gradient term in the micromorphic force. In other words, in the case where $\mathbf{b}^{\mathrm{m}}_{\mathrm{n+1}} = \boldsymbol{A}\cdot\nabla_{\boldsymbol{X}}\tilde{\eta}_{\mathrm{n+1}}$, a special case considered only in this study, the constitutive relation can be simplified as $\mathbf{b}^{\mathrm{m}}_{\mathrm{n+1}} = A^{\mathrm{m}}\nabla_{\boldsymbol{X}}\tilde{\eta}_{\mathrm{n+1}}$ in Eq. (36). Thus, the last diagonal term within the micromorphic global balance is a frame-independent constant.

$$\frac{\partial \mathbf{b}^{\mathrm{m}}}{\partial \nabla_{\boldsymbol{X}}\tilde{\eta}} = A^{\mathrm{m}}\mathbf{1} \tag{81}$$

The following two relations for consistent tangent matrices, including the stress- and strain-gradient terms, received less attention owing to the definition of the Helmholtz free energy in the reference configuration in Eq. (51), which are the off-diagonal Jacobians coupling gradient terms. However, they are not zero in cases such as kinematic hardening.

$$\frac{\partial \mathbf{S}}{\partial \nabla_{\boldsymbol{X}}\tilde{\eta}} = \mathbf{0}, \quad \frac{\partial \mathbf{b}^{\mathrm{m}}}{\partial \mathbf{E}} = \mathbf{0} \tag{82}$$

3.4. Material constitutive response

The first investigation focused on the material behavior at the material point level to verify the non-gradient case of the proposed model. The situation "($\alpha = 1$)" in Eq. (37) was considered, implying that "$f(\mathrm{D}) \equiv \mathrm{h}(\mathrm{D}) = \exp(-\mathrm{D})$" in Watanabe et al. (2008) and Kiefer et al. (2018).

First, the single element under a uniaxial tensile boundary condition of almost 100% strain was investigated. The applied material constant was concluded in Table 1 with ($H^{\mathrm{m}} = 0$), as discussed in previous sections regarding the capacity of the proposed model, including several fracture responses controlled by the critical damage threshold Ψ^{d}_0 and the evolution of damage. Fig. 1(a) shows different stress–strain material responses with Ψ^{d}_0 ranging from 0.1 to 20. The evolution of the effective undamaged variable is referred to as the elastic and plastic degradation functions $f(\mathrm{D})$ and $h(\mathrm{D})$, which range from 1 (undamaged) to 0 (fully damaged). The isotropic damage hardening variable η is shown in Fig. 1(b) and Fig. 1(c). For instance, the green solid line ($\Psi^{\mathrm{d}}_0 = 0.1$) is considerably distinct compared to ($\Psi^{\mathrm{d}}_0 = 10, 20$), similar to the difference between cohesive and ductile fractures. Fig. 1(c) shows that, owing to the same evolution of isotropic damage hardening ($H^{\mathrm{d}} = 5$), the slope should be the same mathematically. This evolution of η is unbounded, similar to the evolution of the plastic hardening variable ξ.

To better understand the proposed model, Fig. 2 shows certain tests with fixed values ($\Psi^{\mathrm{d}}_0 = 0.1, 10, 20$) that can be compared with the results in Fig. 1. The results of different damage hardening modules from ($H^{\mathrm{d}} = 1$) to ($H^{\mathrm{d}} = 300$) were investigated. From Figs. 2(a) and 2(b), the controllable range of the softening effect related to H^{d} has a bound of the slope, owing to the relation with

Table 1
Material constants, where $\boldsymbol{x}$ means comparable changing.

Material constant	Symbol	Unit	Sections				
Elasticity			3.4	4.1.1	4.1.2	4.3	
Young's modulus	E	(GPa)	18.0	210.0	210.0	113.0	
Poisson's ratio	ν	(–)	0.2	0.3	0.3	0.32	
Plasticity						Phase 1	Phase 2
Yield strength	τ_0	(MPa)	20.0	400.0	250.0	830.0	1100.0
Hardening module	H^{p}	(MPa)	–	600.0	2000.0	400.0	200.0
Relative saturated strength	$\delta\tau_{\mathrm{s}}$	(MPa)	12.5	–	–	–	–
Sensitive parameter	q^{p}	(–)	8.5	–	–	–	–
Damage							
Damage energy threshold	Ψ_0^{d}	(mJ/mm^2)	0.1/10/20	150.0	2.0	200.0	
Hardening module	H^{d}	(mJ/mm^2)	$\boldsymbol{x}$	100.0	100.0	100.0	
Micromorphic damage hardening							
Micromorphic module	A^{m}	(mJ)	1.0	100.0	1000.0	$\boldsymbol{x}$	
Coupling parameter	H^{m}	(mJ/mm^2)	0.0/1000.0	10.0	100.0	100.0	
Volume fraction (dp1)						87.6%	12.4%
Volume fraction (dp2)						56.1%	43.9%

an identical elastoplastic material property. Hence, it is easily controlled with a relatively rapid evolution of the damage hardening, as also proven by Brepols et al. (2020). The geometrically nonlinear material response is shown in the reaction force–strain curve in Fig. 2(b).

The micromorphic effect has not being presented so far, owing to the homogeneous state of the isotropic damage hardening variable η, meaning no gradient exists within the field of η. This is why the setting of ($H^{\mathrm{m}} = 0$) is theoretically correct. However, this consideration should be evident from the numerical solution (Ling, 2017). A simple shear test was conducted under almost 100% shear strain, as shown in Fig. 3. The global nonlinear elastoplastic damage problem can be reduced into a linear problem in Eqs. (41) and (42) with ($H^{\mathrm{m}} = 0$) and a different critical damage threshold Ψ_0^{d} condition, as shown in Fig. 3a and c. However, the global nonlinear solution should be completed in accordance with the micromorphic Eq. (44) if ($H^{\mathrm{m}} = 1000$), as shown in Fig. 3b and d. From the homogeneous micromorphic damage hardening variable $\tilde{\eta}$, it will be equal with the isotropic term η, owing to the elimination of the "$a^{\mathrm{m}} = -H^{\mathrm{m}}(\eta - \tilde{\eta})$" in Eq. (16).

4. Numerical examples

Certain heterogeneous numerical examples with linear approximations of discretization for the displacements $\mathbf{u}$ and micromorphic hardening variable $\tilde{\eta}$ are performed in the following sections. The demonstrated structures include a benchmark for the asymmetric double-notch tensile sample and the tensile tests of a plate with a central hole. These are discussed at the engineering scale regarding the damage process and mesh dependency. A schematical discussion about the scale transition in the fracture analysis is presented to define the reasonable characteristic length. Microscopic examples are performed to emphasize the effects of microscopic features and define the length scale during the scale transition in the fracture analysis. All material constants used in further sections are shown in Table 1. The aforementioned finite strain elastoplastic damage model was implemented within the Multiphysics Object Oriented Simulation Environment (MOOSE) (Giudicelli et al., 2024). The parallel finite element discretization was implemented in libMesh (Kirk et al., 2006). The global parallel scalable nonlinear equations and linear equation solvers were performed within the Portable, Extensible Toolkit for Scientific Computation (PETSc) (Balay et al., 2024).

4.1. Example 1: Macroscopic numerical examples

4.1.1. Benchmark: Asymmetric double-notch tensile sample

From different ductile analyses in other works, the double-notch sample under tensile loading conditions presented an asymmetric formation of the damage zone and propagation path. The geometry and boundary condition settings were discussed in previous works (Mediavilla et al., 2006; Aldakheel et al., 2018; Seupel et al., 2018). Fig. 4 shows a three–dimensional perspective. Additionally, material constants for elasticity were modeled similarly to general steel. Linear plastic hardening with a large hardening module H^{p} was considered to avoid material softening–induced plastic hardening. According to the parameters for micromorphic extension, the regularized length of "$l_{\mathrm{c}} = 3.16$ mm" was considered for the mesh size in Fig. 4. Notably, damage initiation occurred where the highly plastic strain was concentrated in Fig. 5a. Further, given tensile loading, a damage zone was formed along an asymmetric path owing to the total elastoplastic energy, shown in Fig. 5b. Additionally, localized inplane-directional shrinking owing to damage accumulation at the surface of a notch can be explained as a significant difference from the two-dimensional structural analysis. Further growth along the damage zone is shown in Fig. 5c. The material response after Fig. 5b was changed to inverse material softening, owing to the shrinking of the damage zone close to the crack path.

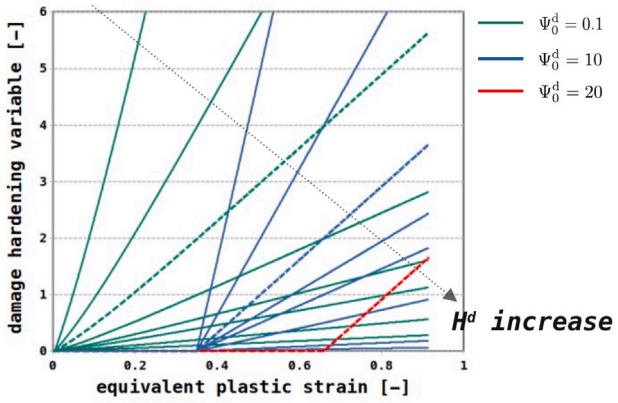

(a) Damage hardening variable η with different H^{d} values; the dashed lines in Figure1c

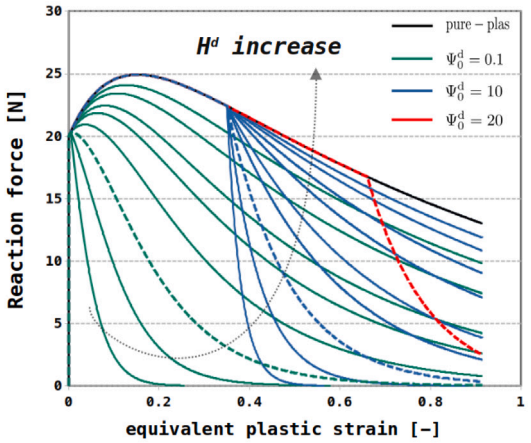

(b) Reaction force–strain curves with different H^{d} values; the dashed lines in Figure1

Fig. 2. Softening by the damage parameter under finite strain. $\Psi_0^{\mathrm{d}} = 20$ in red, $\Psi_0^{\mathrm{d}} = 10$ in blue, and $\Psi_0^{\mathrm{d}} = 0.1$ in green. The pure-plasticity is shown with a black line.

4.1.2. Mesh dependency: Tensile test of a plate with a central hole

The relatively complicated double-notch demonstration shows that damage processes can be characterized with this proposed ductile fracture model. However, it is not sufficient to verify this model with respect to engineering scale problems, as there may be other issues. For example, as another crucial issue induced by localization due to damage, some researchers provided reasonable theoretical explanations as to why the "fake" mesh dependency due to damage was triggered, as written in Section Section 1.1.

To better demonstrate the decrease in mesh dependency with the involved micromorphic extension, cohesive fracture analysis was regarded as a relatively simple material fracture response and performed. The three–dimensional plate with a central hole has the same geometry and uniaxial tensile boundary conditions, as shown in Fig. 6, in accordance with Kiefer et al. (2018). According to material constants, cohesive damage processes can be modeled via adjustments to Table 1 with yield strength parameters of ($\tau_0 \to \infty$) and ($H^{\mathrm{d}} = 20$). Hence, the demonstration of the effective undamaged variable $f, h(\mathrm{D})$ and the reaction force–displacement curve with different mesh sizes from 5824 to 71,920 elements are shown in Fig. 7, which presents the same results across different mesh sizes. The reason is that the regularized length was selected as "$l_{\mathrm{c}} = 3.16$ mm", including all mesh sizes. The results when the wrong regularized length is selected are explained in Miehe et al. (2010) and Sprave and Menzel (2023). Additionally, a smaller mesh size presented a more detailed crack surface via element deletion when the condition of the effective undamaged variable ($f, h(\mathrm{D}) < 0.01$) was satisfied.

Regarding the ductile fracture aspect with material constants in Table 1, the same mesh sizes were used, given displacement control, as shown in Fig. 8. The results of the ductile fracture analysis in Fig. 8(a) show the effective undamaged variable before crack initiation. The regularization effect of the proposed model can be proven via the result that the same damage zones occurred

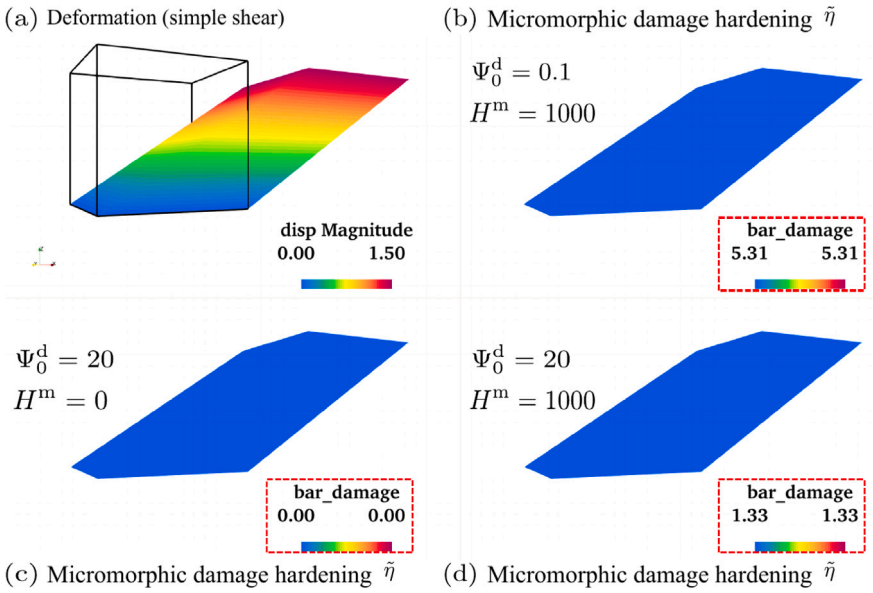

Fig. 3. Homogeneous solutions under a simple shear test. The upper row has $\Psi_0^{\mathrm{d}} = 0.1$, the bottom row has $\Psi_0^{\mathrm{d}} = 20$, the left column has $H^{\mathrm{m}} = 0$, and the right column has $H^{\mathrm{m}} = 1000$.

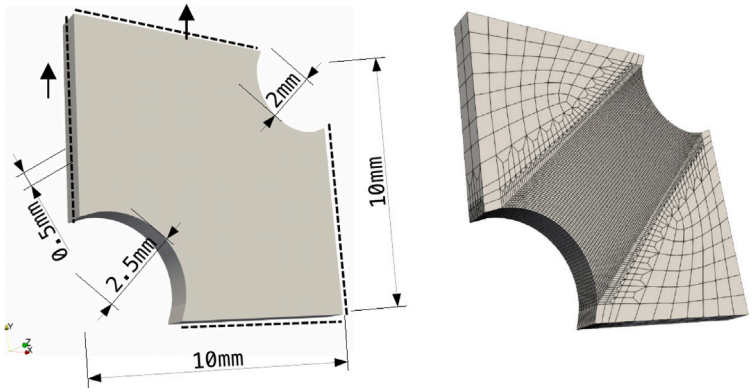

Fig. 4. Geometry, mesh, and boundary conditions of a double-notch sample.

at different mesh sizes, not in one row of elements, as discussed in Wcisło et al. (2013). A crucial discussion exists regarding the spurious damage spreading phenomenon within the application of gradient-enhanced models in the works by Xu and Poh (2019) and Abatour and Forest (2024). This issue was not significant in the ductile fracture analysis shown in Figs. 5 and 8(b). The proposed model maintained the propagation of damage zone growth inside the elasto–plastic zone. The plasticity yield surface shrank when the effective loading surface decreased based on the continuum damage mechanics. The special damage zone of ductile fracture was characterized in Fig. 5b. The beginning of material degradation was independent on mesh refinement. However, a slight distinction arises during further softening, as the plastic behavior in the proposed model is defined in the plastic intermediate configuration. The extension of strain-gradient plasticity can address this issue, particularly in the context of the proposed model.

4.2. Scale transition in fracture analysis

Before discussing numerical examples on the microscopic scale, it is necessary to emphasize the scale transition in fracture analysis via homogenization theory.

According to the classical homogenization theory and its implementation using a computational approach, detailed discussions have been published in Terada et al. (2003), Kouznetsova et al. (2001, 2002), Fish (2013), Zohdi and Wriggers (2004), Schröder (2014), and Watanabe et al. (2005). These sources assumed the material point, which was regarded as the quadrature point within the finite element method. It was assigned by each statistical volume element for numerical material tests, such as the "(a,c) step" of the schematical demonstration in Fig. 9(a). Numerical material tests under the given global constraints can be conducted

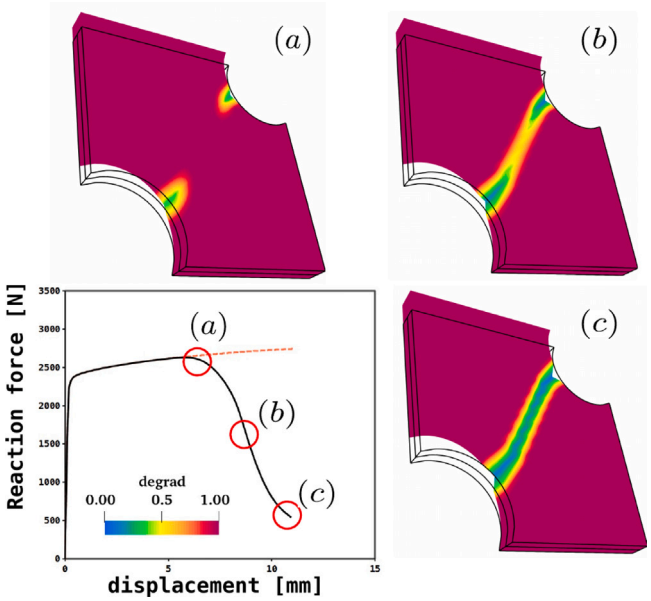

Fig. 5. Conclusions for the numerical results of the double-notch sample. Reaction force displacement curve with a red dashed line for the no damage case. Effective undamaged variable $f, h(\mathrm{D})$ of the damage processes (a,b,c).

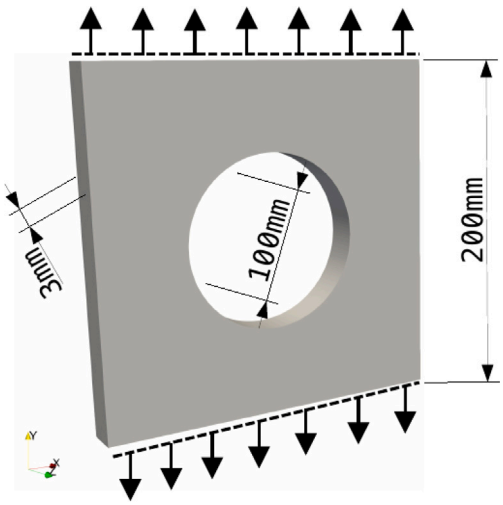

Fig. 6. Geometry and uniaxial tensile boundary conditions of a plate with a hole.

on the microscopic scale to provide a macroscopic effective material response with certain microscopic features. This bottom-up homogenization is presented briefly as follows.

For the Hill–Mandel principle regarding the microscopic nominal stress or first Piola–Kirchhoff stress $\mathbf{P}(\mathbf{Y})$ with position vector $\mathbf{Y}$ at the microscale and with a microscopic displacement of $\mathbf{u}$, the scale transitions are derived.

$$\mathbf{P}^{\mathrm{M}} = \frac{1}{\Omega^{\mathrm{m}}} \int_{\Omega^{\mathrm{m}}} \mathbf{P}(\mathbf{Y})\, d\Omega \tag{83}$$

$$\mathbf{u}(\mathbf{Y}) = \bar{\boldsymbol{H}}\mathbf{Y} + \mathbf{u}^{+/-}(\mathbf{Y}) \tag{84}$$

in which Ω^{m}, $\mathbf{P}^{\mathrm{M}}$, and $\mathbf{u}^{+/-}(\mathbf{Y})$ are the representative microscopic domain, a macroscopic nominal stress resulting from a microscopic simulation, and microscopic displacement fluctuation, respectively. $\bar{\boldsymbol{H}}$ is the macroscopic deformation gradient that constrains the microscopic $\mathbf{F}$, as defined in Eq. (1).

The ductile fracture problem involves the microscopic localization induced by damage degradations, where the standard scale transition cannot be used. This limitation has already been explained in Besson et al. (2009) and Voyiadjis and Song (2020). Additionally, the explicit modeling of composite or porous materials in microscopic characterization extended the standard

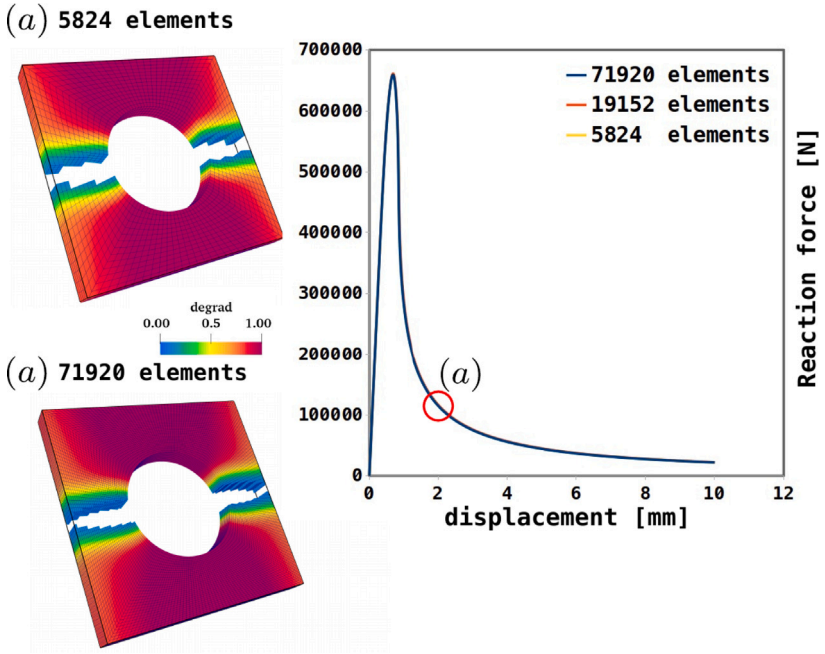

Fig. 7. Conclusions for the numerical cohesive fracture results of a sample plate with a hole. (upper): 5824 elements. (lower): 71,920 elements.

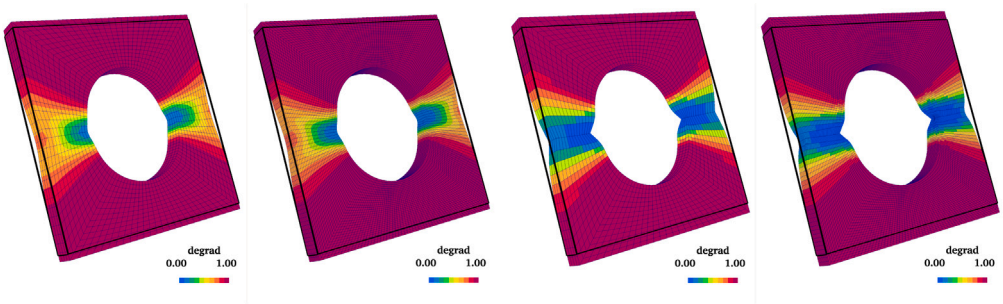

(a) Damage zone $f, h(\mathrm{D})$ before cracking (left): 5,824 (right): 71,120 elements

(b) Damage zone $f, h(\mathrm{D})$ at final (left): 5,824 (right): 71,120 elements

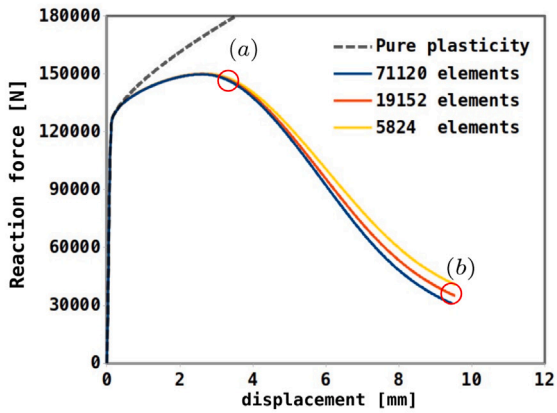

(c) Reaction force–displacement curve

Fig. 8. Conclusions for numerical ductile fracture results of the plate with a hole.

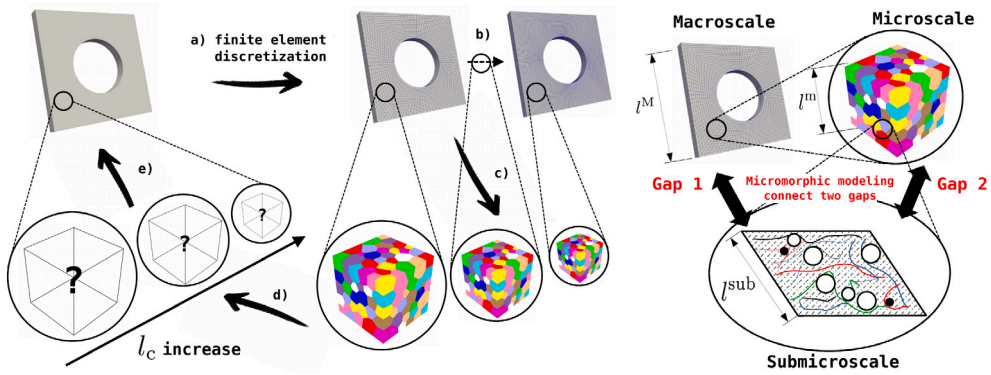

Fig. 9. Schematical framework for the length scale in damaged homogenization. (a) Finite element discretization. (b) Scale changing of microscopic sample. (c) Down–scale transition. (d) Microscopic boundary value problem. (e) Averaging up–scale procedure.

computational homogenization in ductile fracture (Biswas et al., 2019; Coenen et al., 2012), describing the geometrical softening caused by the deformation of voids. However, the above framework is not flexible, particularly for the brittle fracture mechanism, and causes incorrect microscopic localization without extraordinary boundary relaxation.

The proposed bottom-up homogenization extends via definitions of the macroscopic l^{M}, microscopic l^{m}, and submicroscopic characteristic lengths l^{sub}. The proposed assumption that "the micromorphic phenomenon related to micro-cracks on the submicro–scale cannot be observed on both macro–scale (assemble sample) and micro–scale (polycrystals), such as the dislocation structures in plasticity", was presented in Fig. 9(b). Moreover, the discrete submicroscopic mechanism can be characterized via molecular simulation, such as multiscale analysis in the study by Park et al. (2020).

(1) The suitable length scale l_{c} was defined at the same macroscopic global boundary value problem as that shown "from step (b) to step (c)" of Fig. 9(a). The $\tilde{\eta}$ and $\tilde{\eta}^{+/-}$ are the micromorphic damage hardening and its fluctuation, respectively, whereas the $\nabla^{\mathrm{M}}_{\boldsymbol{X}}\tilde{\eta}\left(l^{\mathrm{M}}\right)$ term came from the macroscopic boundary value problem with a macroscopic l^{M} and position vector with microscopic characteristic lengths of l^{m}.

$$\tilde{\eta} = \nabla^{\mathrm{M}}_{\boldsymbol{X}}\tilde{\eta}\left(l^{\mathrm{M}}\right)\mathbf{Y}\left(l^{\mathrm{m}}\right) + \tilde{\eta}^{+/-} \tag{85}$$

(2) Macroscopic global constraints with macroscopic characteristic length lead to "size–dependent" microscopic problems with the micromorphic Eqs. (16) and (40), as shown in step (d) of Fig. 9(a). Micromorphic conjugate forces $(\bullet)^{\mathrm{m}}$ and macroscopic components $(\bullet)^{\mathrm{M}}$ can be derived.

$$\mathbf{b}^{\mathrm{M}} = \frac{1}{\Omega^{\mathrm{m}}}\int_{\Omega^{\mathrm{m}}}\left(l^{\mathrm{M}} - l^{\mathrm{m}}\right)\mathbf{b}^{\mathrm{m}}(\mathbf{Y})\,d\Omega \tag{86}$$

$$a^{\mathrm{M}} = \frac{1}{\Omega^{\mathrm{m}}}\int_{\Omega^{\mathrm{m}}} l^{\mathrm{m}}(\tilde{\eta} - \eta)\,d\Omega \tag{87}$$

Additionally, the macroscopic boundary value problem changes with the suitable definition of the normalized overlapping term $\left(\delta_{\mathrm{c}} = \sqrt{\left(l^{\mathrm{M}} - l^{\mathrm{m}}\right)/l^{\mathrm{m}}}\right)$, which connects the scale transition between the two-scales to characterize different gaps with respect to the submicro–scale. Moreover, the length scale is defined as $\left(l_{\mathrm{c}} = \delta_{\mathrm{c}} l^{\mathrm{sub}}\right)$ in Eq. (40), as shown in Fig. 9(b). Importantly, the imaged size of the statistical volume element increases with a decreasing l_{c}. The condition $\left(l_{\mathrm{c}} = 0,\ l^{\mathrm{M}} \approx l^{\mathrm{m}} \gg l^{\mathrm{sub}}\right)$ and $\left(l^{\mathrm{M}} \gg l^{\mathrm{m}} \approx l^{\mathrm{sub}} \approx 0, \nabla_{\boldsymbol{X}}\tilde{\eta} = 0\right)$ were held in classical homogenization theory, which assumed total scale separation. The derivation is discussed in other multi-physics problems by de Souza Neto et al. (2015) and Waseem et al. (2020).

4.3. Example 2 (length scale): Duplex microstructures

The numerical tests on microstructures were performed about the length scale l_{c} definition, owing to the comprehensive physical meaning provided in extended homogenization theory. Fig. 10 shows a microscopic inclusion–matrix system characterized by duplex virtual microstructures with a soft phase 1 (blue) and hard phase 2 (red), with different volume fractions and a randomly hard phase 2 distribution as inclusion. The material constants used for phases are shown in Table 1.

4.3.1. Characterization of microscopic shear bands with "$\left(l^{\mathrm{M}} - l^{\mathrm{m}}\right) = 0.01$"

The definition of the length scale must fix one side of the characteristic length on either the microscale l^{m} or the macroscale l^{M}. The preliminary condition ($l^{\mathrm{m}} = l^{\mathrm{sub}} = 1$) is satisfied for all simulations. The first result considers the global kinematic constraint via the macroscopic displacement gradient $\bar{H}_{\mathrm{xx}}$ and the identical submicroscopic damage hardening, which can be achieved in

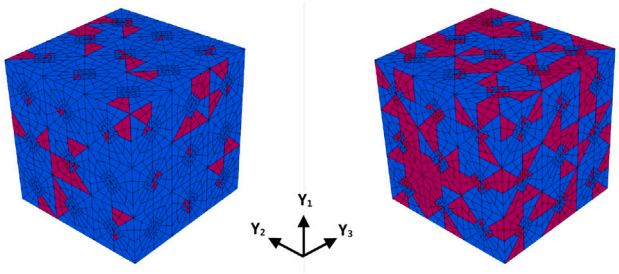

(a) Two duplex microstructures

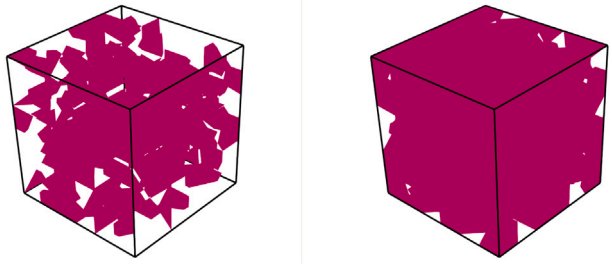

(b) Randomly hard phase distribution

Fig. 10. Geometry and volume fraction of duplex microstructures Left: dp1, Right: dp2.

Fig. 11(c) and is shown in Figs. 11(a) and 11(b) for the effective undamaged variable $f, h(\mathrm{D})$ and the global micromorphic damage hardening variable $\tilde{\eta}$ when ($l^{\mathrm{M}} = 1.01$). Clearly, microscopic shear bands are presented within numerical material tests in Fig. 11(a). Additionally, the correct characterization of damage localization can be achieved in the presented homogenization framework in microstructures. For the yield point phenomenon in the plastic softening case, the homogenization framework provided a phenomenological explanation for the microscopic strain localization induced by the yield-point stress-drop, as discussed by Yanagawa and Watanabe (2024). On the other hand, the discussion, including clear microscopic shear bands, is presented within numerical material tests. However, the different fracture modes in two duplex microstructures are characterized by distinctive microscopic damage, which can be explained by the spatial distribution of the hard phase 2 in Fig. 10. When the relation ($l^{\mathrm{M}} = 1.01$) is considered, it means that the current length scale can be utilized to characterize a large macroscopic material response corresponding to the large microstructure in Fig. 9(a). The slightly macroscopic anisotropic damage property is proven, as shown in Fig. 11(c). A detailed discussion of different loading directions is provided in Appendix.

4.3.2. Definitions of length scale with "$\left(l^{\mathrm{M}} - l^{\mathrm{m}}\right) = x$"

Certain previous preliminaries remained in the second analysis, including ($l^{\mathrm{m}} = l^{\mathrm{sub}} = 1$), which presented the fixed submicro/microscopic characteristic lengths. The same global constraint from the macroscopic displacement gradient $\bar{H}_{\mathrm{xx}}$ was shown for the macroscopic material responses in Figs. 12(c) and 12(d). The key point used to investigate the variation of the length scale l_{c} by the macroscopic characteristic length ($l^{\mathrm{M}} = 2/1.1/1.01$) was assigned by the material constants of 1% of the length scale with a variant A^{m} and a fixed ($H^{\mathrm{m}} = 100$), as shown in Table 1. As discussed in the case ($l^{\mathrm{M}} = 1.01$), this microstructure can characterize fully microscopic shear bands induced by damage. However, the same macroscopic damage material response without micromorphic extension is not reasonable for ductile fracture analysis with an increased length scale, as shown in Fig. 9(a). The definition of the suitable length scale should be considered in the scale transition to the macroscale and regarded as the answer to "questions" in Fig. 9(a). Slightly changing the length scale causes different results for the microscopic boundary value problem. The localization of damage within the microscopic shear band induces less ductility of materials, which is controlled by overlapping the macroscopic and microscopic characteristic lengths from homogeneous to highly localized states. As noted in Notes 5 and 7, the results in Fig. 12(b) coincide with the physical meanings regarding the global damage hardening variable $\tilde{\eta}$. It reaches the homogeneous state in the first result of Fig. 12(b) when the macroscale is relatively larger than the microscale. In other words, the capacity of the microstructure to characterize more information and transfer it back to the macroscale can be better explained when enough of the microscale is compared with the macroscale. Hence, the result of this study is that the "δ_{c}" term that describes the normalized overlapping of the characteristic lengths in Eq. (86) is phenomenologically explained as the width of the microscopic shear band (strain localization) due to damage. Additionally, the length scale l_{c} is explained as the size of the microstructure with respect to the submicro–scale.

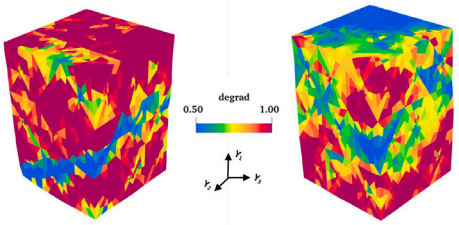

(a) Damage zone above 20% strain along the Y_1 direction with $l_c = 0.1$ Left:dp2. Right:dp1

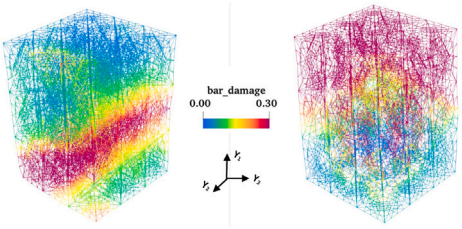

(b) Microscopic damage response $\tilde{\eta}$ above 20% strain along the Y_1 direction with $l_c = 0.1$ Left:dp2. Right:dp1

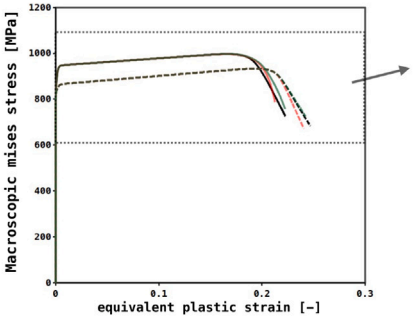

(c) Stress-strain curve with dp1, dp2(dashed, solid line) with $l_c = 0.1$

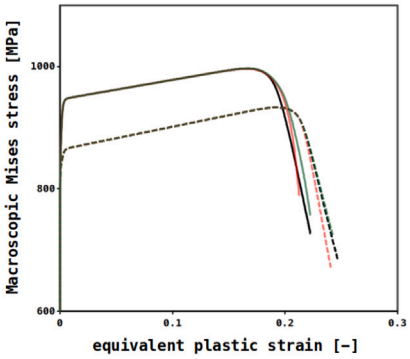

(d) Zoomed-in view of (c) along Y_1(red)/Y_2(green)/Y_3(black)

Fig. 11. (a) Effective undamaged variable $f, h(D)$. (b) Microscopic damage hardening response $\tilde{\eta}$. (c and d) macroscopic material response in two duplex microstructures.

5. Conclusions

The following conclusions are drawn from this study.

1. The extension of the finite strain elastoplastic damage model based on Watanabe et al. (2008) to consider the plastic contribution in ductile fracture analysis as a "non-gradient" model was completed. Fully implicit modeling to capture the gradients of the isotropic damage hardening variable η based on micromorphic theory (Forest, 2009) was proposed.
2. The extended "two-scale" homogenization is considered a suitable definition of the length scale. It provided a reasonable physical meaning to the micromorphic extended model, in which the microvariable was explained as the indicator of the micromorphic damage hardening mechanism.
3. This proposed model can be used to capture the damage process with an asymmetric crack path in a double-notch sample. As the first application of the gradient-enhanced damage model on an engineering scale, the cohesive and ductile fracture analysis with different mesh sizes proved that the proposed model can decrease mesh dependency. However, a slight difference exists in terms of further crack propagation due to plastic strain localization. This may be resolved via coupling with strain-gradient plasticity in the future.
4. The physical definition of the length scale during the bottom-up scale transition using duplex microstructures with different volume fractions was examined. The overlapping of the "two-scale" characteristic lengths expressed the width of the microscopic shear bands in the proposed damage model. Additionally, the length scale can be explained via the size of the microstructure.

In terms of limitations and future work, the proposed model is an essential starting point in ductile fracture analysis. Further model validation with advanced experiments, particularly in different scale characterizations, is required. Coupling with single crystal plasticity within polycrystalline ductile materials is required to characterize detailed microstructural features. Moreover, robustness and computational efficiency are significant in more complicated ductile fracture analysis.

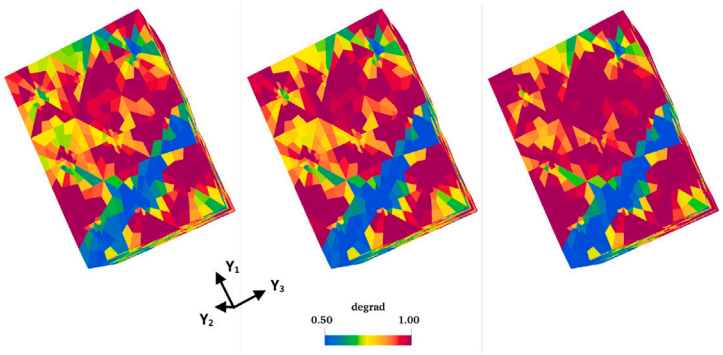

(a) Damage zone with $l_c = 1/0.3/0.1$ along the Y_1 direction

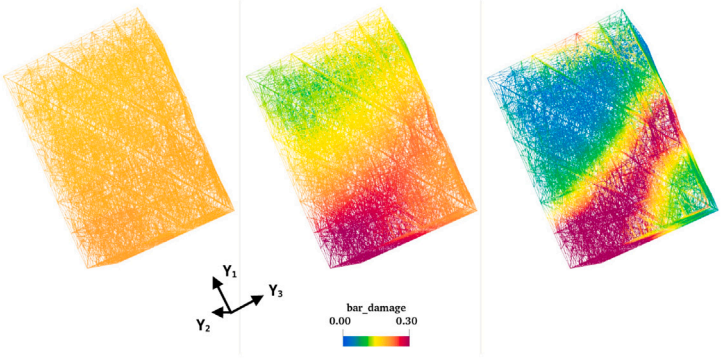

(b) Microscopic damage response $\tilde{\eta}$ with $l_c = 1/0.3/0.1$

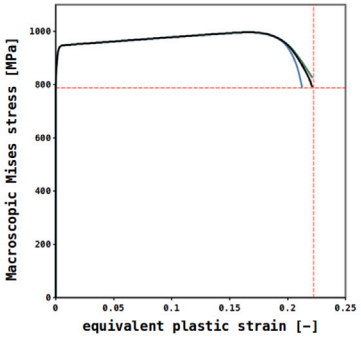

(c) Stress-strain curve 1(green)/0.3(black)/0.1(blue)

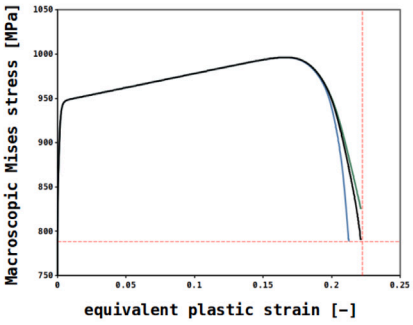

(d) Zoomed-in view of (c) 1(green)/0.3(black)/0.1(blue)

Fig. 12. (a) Effective undamaged variable $f, h(\mathrm{D})$. (b) Microscopic damage hardening response $\tilde{\eta}$. (c and d) Macroscopic material response in dp1 duplex microstructures.

CRediT authorship contribution statement

Tianwen Tan: Writing – original draft, Validation, Methodology, Investigation, Formal analysis. **Ikumu Watanabe:** Writing – original draft, Supervision, Resources, Project administration, Methodology, Investigation, Funding acquisition, Conceptualization.

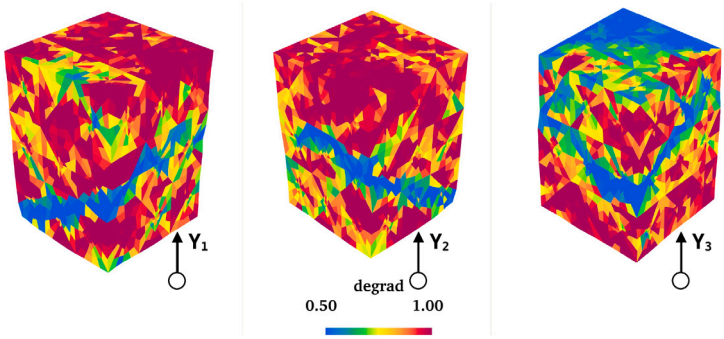

(a) Damage zone above 20% strain along $Y_1/Y_2/Y_3$

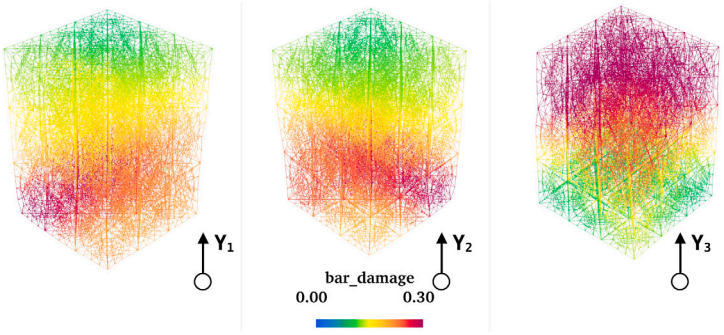

(b) Microscopic damage hardening response $\tilde{\eta}$ with $l_c = 0.3$

Fig. A.1. (a) Effective undamaged variable $f, h(D)$. (b) Microscopic damage hardening response $\tilde{\eta}$ in dp2 duplex microstructures.

Declaration of competing interest

The authors declare that they have no known competing financial interests or personal relationships that could have appeared to influence the work reported in this paper.

Acknowledgments

This work was partly supported by the Japan Science and Technology Agency (JST) CREST grant number JPMJCR1995, Japan. We would like to thank Editage for English language editing.

Appendix. Dependency of loading direction

The variation of loading direction $Y_1/Y_2/Y_3$ resulted in a slight anisotropic property, as shown in Fig. 11(c), owing to the randomly spatial distribution of hard phase within duplex microstructures. Additional numerical demonstrations for the $Y_1/Y_2/Y_3$ loading directions under global damage hardening conditions with ($l_c = 0.3$) are shown in Fig. A.1. The microscopic characterization of shear bands varied with the loading direction and control macroscopic ductile fracture material property.

Data availability

Data will be made available on request.

References

Abatour, M., Forest, S., 2024. Strain gradient plasticity based on saturating variables. Eur. J. Mech. A Solids 104, 105016.
Aifantis, E.C., 1987. The physics of plastic deformation. Int. J. Plast. 3 (3), 211–247.
Aldakheel, F., Wriggers, P., Miehe, C., 2018. A modified Gurson-type plasticity model at finite strains: formulation, numerical analysis and phase-field coupling. Comput. Mech. 62, 815–833.
Ambati, M., Kruse, R., De Lorenzis, L., 2016. A phase-field model for ductile fracture at finite strains and its experimental verification. Comput. Mech. 57, 149–167.

Aslan, O., Cordero, N., Gaubert, A., Forest, S., 2011b. Micromorphic approach to single crystal plasticity and damage. Internat. J. Engrg. Sci. 49 (12), 1311–1325.
Aslan, O., Quilici, S., Forest, S., 2011a. Numerical modeling of fatigue crack growth in single crystals based on microdamage theory. Int. J. Damage Mech. 20 (5), 681–705.
Balay, S., Abhyankar, S., Adams, M.F., Benson, S., Brown, J., Brune, P., Buschelman, K., Constantinescu, E.M., Dalcin, L., Dener, A., Eijkhout, V., Faibussowitsch, J., Gropp, W.D., Hapla, V., Isaac, T., Jolivet, P., Karpeev, D., Kaushik, D., Knepley, M.G., Kong, F., Kruger, S., May, D.A., McInnes, L.C., Mills, R.T., Mitchell, L., Munson, T., Roman, J.E., Rupp, K., Sanan, P., Sarich, J., Smith, B.F., Zampini, S., Zhang, H., Zhang, H., Zhang, J., 2024. PETSc web page. URL: https://petsc.org/, https://petsc.org/.
Bao, Y., Wierzbicki, T., 2004. On fracture locus in the equivalent strain and stress triaxiality space. Int. J. Mech. Sci. 46 (1), 81–98.
Bažant, Z.P., 1987. Why continuum damage is nonlocal: justification by quasiperiodic microcrack array. Mech. Res. Commun. 14 (5–6), 407–419.
Bazant, Z.P., Belytschko, T.B., Chang, T.-P., et al., 1984. Continuum theory for strain-softening. J. Eng. Mech. 110 (12), 1666–1692.
Bazant, Z.P., Pijaudier-Cabot, G., 1988. Nonlocal continuum damage, localization instability and convergence.
Belytschko, T., Liu, W.K., Moran, B., Elkhodary, K., 2014. Nonlinear Finite Elements for Continua and Structures. John wiley & sons.
Besson, J., 2010. Continuum models of ductile fracture: a review. Int. J. Damage Mech. 19 (1), 3–52.
Besson, J., Cailletaud, G., Chaboche, J.-L., Forest, S., 2009. Non-Linear Mechanics of Materials, vol. 167, Springer Science & Business Media.
Biswas, R., Shedbale, A., Poh, L., 2019. Nonlinear analyses with a micromorphic computational homogenization framework for composite materials. Comput. Methods Appl. Mech. Engrg. 350, 362–395.
Boffi, D., Brezzi, F., Fortin, M., et al., 2013. Mixed Finite Element Methods and Applications, vol. 44, Springer.
Brepols, T., Wulfinghoff, S., Reese, S., 2020. A gradient-extended two-surface damage-plasticity model for large deformations. Int. J. Plast. 129, 102635.
Chaboche, J.-L., 1978. Description thermodynamique et phénoménologique de la viscoélasticité cyclique avec endommagement.
Chen, Y., 2019. Modeling of Ductile Fracture Using Local Approach: Reliable Simulation of Crack Extension (Ph.D. thesis). Université Paris sciences et lettres.
Coenen, E., Kouznetsova, V., Bosco, E., Geers, M., 2012. A multi-scale approach to bridge microscale damage and macroscale failure: a nested computational homogenization-localization framework. Int. J. Fract. 178, 157–178.
De Borst, R., Crisfield, M.A., Remmers, J.J., Verhoosel, C.V., 2012. Nonlinear Finite Element Analysis of Solids and Structures. John Wiley & Sons.
De Borst, R., Sluys, L.J., Muhlhaus, H.-B., Pamin, J., 1993. Fundamental issues in finite element analyses of localization of deformation. Eng. Comput. 10 (2), 99–121.
de Souza Neto, E.A., Blanco, P.J., Sánchez, P.J., Feijóo, R.A., 2015. An RVE-based multiscale theory of solids with micro-scale inertia and body force effects. Mech. Mater. 80, 136–144.
de Souza Neto, E., Perić, D., Dutko, M., Owen, D., 1996. Design of simple low order finite elements for large strain analysis of nearly incompressible solids. Int. J. Solids Struct. 33 (20–22), 3277–3296.
de Souza Neto, E., Perić, D., Owen, D., 1998. Continuum modelling and numerical simulation of material damage at finite strains. Arch. Comput. Methods Eng. 5, 311–384.
de Souza Neto, E.A., Peric, D., Owen, D.R., 2011. Computational Methods for Plasticity: Theory and Applications. John Wiley & Sons.
Desmorat, R., Cantournet, S., 2008. Modeling microdefects closure effect with isotropic/anisotropic damage. Int. J. Damage Mech. 17 (1), 65–96.
Diamantopoulou, E., Liu, W., Labergere, C., Badreddine, H., Saanouni, K., Hu, P., 2017. Micromorphic constitutive equations with damage applied to metal forming. Int. J. Damage Mech. 26 (2), 314–339.
Dimitrijevic, B.J., Hackl, K., 2011. A regularization framework for damage–plasticity models via gradient enhancement of the free energy. Int. J. Numer. Methods Biomed. Eng. 27 (8), 1199–1210.
Eringen, A.C., 2001. Microcontinuum Field Theories: I I. Fluent Media, vol. 2, Springer Science & Business Media.
Felder, S., Kopic-Osmanovic, N., Holthusen, H., Brepols, T., Reese, S., 2022. Thermo-mechanically coupled gradient-extended damage-plasticity modeling of metallic materials at finite strains. Int. J. Plast. 148, 103142.
Fish, J., 2013. Practical Multiscaling. John Wiley & Sons.
Forest, S., 2009. Micromorphic approach for gradient elasticity, viscoplasticity, and damage. J. Eng. Mech. 135 (3), 117–131.
Forest, S., 2016. Nonlinear regularization operators as derived from the micromorphic approach to gradient elasticity, viscoplasticity and damage. Proc. R. Soc. A 472 (2188), 20150755.
Giudicelli, G., Lindsay, A., Harbour, L., Icenhour, C., Li, M., Hansel, J.E., German, P., Behne, P., Marin, O., Stogner, R.H., Miller, J.M., Schwen, D., Wang, Y., Munday, L., Schunert, S., Spencer, B.W., Yushu, D., Recuero, A., Prince, Z.M., Nezdyur, M., Hu, T., Miao, Y., Jung, Y.S., Matthews, C., Novak, A., Langley, B., Truster, T., Nobre, N., Alger, B., Andrš, D., Kong, F., Carlsen, R., Slaughter, A.E., Peterson, J.W., Gaston, D., Permann, C., 2024. 3.0 - MOOSE: Enabling massively parallel multiphysics simulations. SoftwareX 26, 101690. http://dx.doi.org/10.1016/j.softx.2024.101690, URL: https://www.sciencedirect.com/science/article/pii/S235271102400061X.
Gurson, A.L., 1977. Continuum theory of ductile rupture by void nucleation and growth: Part I—Yield criteria and flow rules for porous ductile media.
Gurtin, M.E., 2002. A gradient theory of single-crystal viscoplasticity that accounts for geometrically necessary dislocations. J. Mech. Phys. Solids 50 (1), 5–32.
Gurtin, M.E., Fried, E., Anand, L., 2010. The Mechanics and Thermodynamics of Continua. Cambridge University Press.
Hütter, G., 2017. A micromechanical gradient extension of Gurson's model of ductile damage within the theory of microdilatational media. Int. J. Solids Struct. 110, 15–23.
Johnson, G.R., Cook, W.H., 1985. Fracture characteristics of three metals subjected to various strains, strain rates, temperatures and pressures. Eng. Fract. Mech. 21 (1), 31–48.
Kachanov, L., 1958. Time of the rupture process under creep conditions. TX. Akad. Nauk. SSR. Otd. Tekh. 8 (26), 31.
Kattan, P.I., Voyiadjis, G.Z., 2012. Damage Mechanics with Finite Elements: Practical Applications with Computer Tools. Springer Science & Business Media.
Kiefer, B., Waffenschmidt, T., Sprave, L., Menzel, A., 2018. A gradient-enhanced damage model coupled to plasticity—multi-surface formulation and algorithmic concepts. Int. J. Damage Mech. 27 (2), 253–295.
Kirk, B.S., Peterson, J.W., Stogner, R.H., Carey, G.F., 2006. libMesh: A C++ Library for Parallel Adaptive Mesh Refinement/Coarsening Simulations. Eng. Comput. 22 (3–4), 237–254. http://dx.doi.org/10.1007/s00366-006-0049-3.
Kouznetsova, V., Brekelmans, W., Baaijens, F., 2001. An approach to micro-macro modeling of heterogeneous materials. Comput. Mech. 27 (1), 37–48.
Kouznetsova, V., Geers, M.G., Brekelmans, W.M., 2002. Multi-scale constitutive modelling of heterogeneous materials with a gradient-enhanced computational homogenization scheme. Int. J. Numer. Methods Eng. 54 (8), 1235–1260.
Leblond, J., Perrin, G., Devaux, J., 1994. Bifurcation effects in ductile metals with nonlocal damage.
Lemaitre, J., 1984. A three-dimensional ductile damage model applied to deep-drawing forming limits. In: Mechanical Behaviour of Materials. Elsevier, pp. 1047–1053.
Lemaitre, J., 2012. A Course on Damage Mechanics. Springer science & business media.
Lemaitre, J., Desmorat, R., Sauzay, M., 2000. Anisotropic damage law of evolution. Eur. J. Mech. A Solids 19 (2), 187–208.
Liebe, T., Steinmann, P., 2001. Theory and numerics of a thermodynamically consistent framework for geometrically linear gradient plasticity. Internat. J. Numer. Methods Engrg. 51 (12), 1437–1467.
Ling, C., 2017. Modeling the intragranular ductile fracture of irradiated steels, Effects of crystal anisotropy and strain gradient (Theses). PSL Research University, URL: https://pastel.archives-ouvertes.fr/tel-01699226.

Ling, C., Forest, S., Besson, J., Tanguy, B., Latourte, F., 2018. A reduced micromorphic single crystal plasticity model at finite deformations. Application to strain localization and void growth in ductile metals. Int. J. Solids Struct. 134, 43–69.
Mediavilla, J., Peerlings, R., Geers, M., 2006. A robust and consistent remeshing-transfer operator for ductile fracture simulations. Comput. Struct. 84 (8–9), 604–623.
Miehe, C., Schaenzel, L.-M., Ulmer, H., 2015. Phase field modeling of fracture in multi-physics problems. Part I. balance of crack surface and failure criteria for brittle crack propagation in thermo-elastic solids. Comput. Methods Appl. Mech. Engrg. 294, 449–485.
Miehe, C., Welschinger, F., Hofacker, M., 2010. Thermodynamically consistent phase-field models of fracture: Variational principles and multi-field FE implementations. Int. J. Numer. Methods Eng. 83 (10), 1273–1311.
Moës, N., Belytschko, T., 2002. Extended finite element method for cohesive crack growth. Eng. Fract. Mech. 69 (7), 813–833.
Nahshon, K., Hutchinson, J., 2008. Modification of the Gurson model for shear failure. Eur. J. Mech. A Solids 27 (1), 1–17.
Neff, P., Ghiba, I.-D., Madeo, A., Placidi, L., Rosi, G., 2014. A unifying perspective: the relaxed linear micromorphic continuum. Contin. Mech. Thermodyn. 26, 639–681.
Neuner, M., Gamnitzer, P., Hofstetter, G., 2020. A 3D gradient-enhanced micropolar damage-plasticity approach for modeling quasi-brittle failure of cohesive-frictional materials. Comput. Struct. 239, 106332.
Neuner, M., Regueiro, R.A., Linder, C., 2022. A unified finite strain gradient-enhanced micropolar continuum approach for modeling quasi-brittle failure of cohesive-frictional materials. Int. J. Solids Struct. 254, 111841.
Oden, J.T., Demkowicz, L., 2017. Applied Functional Analysis. Chapman and Hall/CRC.
Ohno, N., Okumura, D., 2007. Higher-order stress and grain size effects due to self-energy of geometrically necessary dislocations. J. Mech. Phys. Solids 55 (9), 1879–1898.
Park, C., Jung, J., Yun, G.J., 2020. Multiscale micromorphic theory compatible with MD simulations in both time-scale and length-scale. Int. J. Plast. 129, 102680.
Peerlings, R.H., de Borst, R., Brekelmans, W., De Vree, J., 1995. Computational modelling of gradient-enhanced damage for fracture and fatigue problems. In: Computational Plasticity: Fundamentals and Applications: Proceedings of the 4th International Conference Held in Barcelona, Spain, 3-6 April 1995. Pineridge Press, pp. 975–986.
Peerlings, R.H., de Borst, R., Brekelmans, W., Geers, M.G., 1998. Gradient-enhanced damage modelling of concrete fracture. Mech. Cohes. Frict. Mater.: Int. J. Exp. Model. Comput. Mater. Struct. 3 (4), 323–342.
Peerlings, R.H., Geers, M.G., de Borst, R., Brekelmans, W., 2001. A critical comparison of nonlocal and gradient-enhanced softening continua. Int. J. Solids Struct. 38 (44–45), 7723–7746.
Pham, K., Kouznetsova, V.G., Geers, M.G., 2013. Transient computational homogenization for heterogeneous materials under dynamic excitation. J. Mech. Phys. Solids 61 (11), 2125–2146.
Pires, F.A., de Sá, J.C., Sousa, L.C., Jorge, R.N., 2003. Numerical modelling of ductile plastic damage in bulk metal forming. Int. J. Mech. Sci. 45 (2), 273–294.
Rabotnov, Y.N., 1963. Paper 68: On the equation of state of creep. In: Proceedings of the Institution of Mechanical Engineers, Conference Proceedings. Vol. 178, SAGE Publications Sage UK: London, England, pp. 2–117.
Schröder, J., 2014. A numerical two-scale homogenization scheme: the FE2-method. In: Plasticity and beyond: Microstructures, Crystal-Plasticity and Phase Transitions. Springer, pp. 1–64.
Seupel, A., Hütter, G., Kuna, M., 2018. An efficient FE-implementation of implicit gradient-enhanced damage models to simulate ductile failure. Eng. Fract. Mech. 199, 41–60.
Simo, J.C., Ju, J., 1987. Strain-and stress-based continuum damage models—I. Formulation. Int. J. Solids Struct. 23 (7), 821–840.
Sprave, L., Menzel, A., 2020. A large strain gradient-enhanced ductile damage model: finite element formulation, experiment and parameter identification. Acta Mech. 231 (12), 5159–5192.
Sprave, L., Menzel, A., 2023. A large strain anisotropic ductile damage model—Effective driving forces and gradient-enhancement of damage vs. plasticity. Comput. Methods Appl. Mech. Engrg. 416, 116284.
Terada, K., Saiki, I., Matsui, K., Yamakawa, Y., 2003. Two-scale kinematics and linearization for simultaneous two-scale analysis of periodic heterogeneous solids at finite strain. Comput. Methods Appl. Mech. Engrg. 192 (31–32), 3531–3563.
Terada, K., Watanabe, I., 2007. Computational aspects of tangent moduli tensors in rate-independent crystal elastoplasticity. Comput. Mech. 40, 497–511.
Tvergaard, V., Needleman, A., 1984. Analysis of the cup-cone fracture in a round tensile bar. Acta Metall. 32 (1), 157–169.
Upadhyay, M.V., Capolungo, L., Taupin, V., Fressengeas, C., 2013. Elastic constitutive laws for incompatible crystalline media: the contributions of dislocations, disclinations and G-disclinations. Phil. Mag. 93 (7), 794–832.
Voyiadjis, G.Z., Kattan, P.I., 1992. A plasticity-damage theory for large deformation of solids—I. theoretical formulation. Internat. J. Engrg. Sci. 30 (9), 1089–1108.
Voyiadjis, G.Z., Kattan, P.I., 2014. How a singularity forms in continuum damage mechanics. Mech. Res. Commun. 55, 86–88.
Voyiadjis, G.Z., Shojaei, A., Li, G., 2012. A generalized coupled viscoplastic–viscodamage–viscohealing theory for glassy polymers. Int. J. Plast. 28 (1), 21–45.
Voyiadjis, G.Z., Song, Y., 2020. Gradient-Enhanced Continuum Plasticity. Elsevier.
Voyiadjis, G., Yaghoobi, M., 2019. Size Effects in Plasticity: from Macro to Nano. Academic Press.
Waseem, A., Heuze, T., Stainier, L., Geers, M., Kouznetsova, V., 2020. Model reduction in computational homogenization for transient heat conduction. Comput. Mech. 65, 249–266.
Watanabe, I., Terada, K., Akiyama, M., 2005. Two-scale analysis for deformation-induced anisotropy of polycrystalline metals. Comput. Mater. Sci. 32 (2), 240–250.
Watanabe, I., Terada, K., de Souza Neto, E.A., Perić, D., 2008. Characterization of macroscopic tensile strength of polycrystalline metals with two-scale finite element analysis. J. Mech. Phys. Solids 56 (3), 1105–1125.
Wcisło, B., Pamin, J., Kowalczyk-Gajewska, K., 2013. Gradient-enhanced damage model for large deformations of elastic-plastic materials. Arch. Mech. 65 (5), 407–428.
Wriggers, P., 2008. Nonlinear Finite Element Methods. Springer Science & Business Media.
Xu, Y., Poh, L.H., 2019. Localizing gradient-enhanced Rousselier model for ductile fracture. Internat. J. Numer. Methods Engrg. 119 (9), 826–851.
Xue, L., 2007. Damage accumulation and fracture initiation in uncracked ductile solids subject to triaxial loading. Int. J. Solids Struct. 44 (16), 5163–5181.
Xue, L., 2008. Constitutive modeling of void shearing effect in ductile fracture of porous materials. Eng. Fract. Mech. 75 (11), 3343–3366.
Yanagawa, S., Watanabe, I., 2024. Multiscale finite element analysis of yield-point phenomenon in Ferrite–Pearlite duplex steels. ISIJ Int. 64 (5), 874–880.
Zhang, Y., Lorentz, E., Besson, J., 2018. Ductile damage modelling with locking-free regularised GTN model. Internat. J. Numer. Methods Engrg. 113 (13), 1871–1903.
Zhou, J., Gao, X., Sobotka, J.C., Webler, B.A., Cockeram, B.V., 2014. On the extension of the Gurson-type porous plasticity models for prediction of ductile fracture under shear-dominated conditions. Int. J. Solids Struct. 51 (18), 3273–3291.
Zienkiewicz, O.C., Taylor, R.L., Zhu, J.Z., 2005. The Finite Element Method: Its Basis and Fundamentals. Elsevier.
Zohdi, T.I., Wriggers, P., 2004. An Introduction to Computational Micromechanics, vol. 20, Springer Science & Business Media.